

See discussions, stats, and author profiles for this publication at: <https://www.researchgate.net/publication/280628808>

# Electrophoretic Transport of Single DNA Nucleotides Through Nanoslits: A Molecular Dynamics Simulation Study

ARTICLE *in* THE JOURNAL OF PHYSICAL CHEMISTRY B · AUGUST 2015

Impact Factor: 3.3 · DOI: 10.1021/acs.jpcb.5b02798 · Source: PubMed

---

READS

51

## 6 AUTHORS, INCLUDING:



Brian Ray Novak

Louisiana State University

15 PUBLICATIONS 182 CITATIONS

[SEE PROFILE](#)



Kumuditha Ratnayake

University of North Carolina at Chapel Hill

9 PUBLICATIONS 5 CITATIONS

[SEE PROFILE](#)



Steven Soper

Louisiana State University

201 PUBLICATIONS 5,506 CITATIONS

[SEE PROFILE](#)



Dorel Moldovan

Louisiana State University

65 PUBLICATIONS 902 CITATIONS

[SEE PROFILE](#)

# Electrophoretic Transport of Single DNA Nucleotides through Nanoslits: A Molecular Dynamics Simulation Study

Kai Xia,<sup>†</sup> Brian R. Novak,<sup>†</sup> Kumuditha M. Weerakoon-Ratnayake,<sup>‡,||</sup> Steven A. Soper,<sup>§,||,⊥</sup> Dimitris E. Nikitopoulos,<sup>†</sup> and Dorel Moldovan<sup>\*,†</sup>

<sup>†</sup>Department of Mechanical and Industrial Engineering, Louisiana State University, Baton Rouge, Louisiana 70803, United States

<sup>‡</sup>Department of Chemistry, Louisiana State University, Baton Rouge, Louisiana 70803, United States

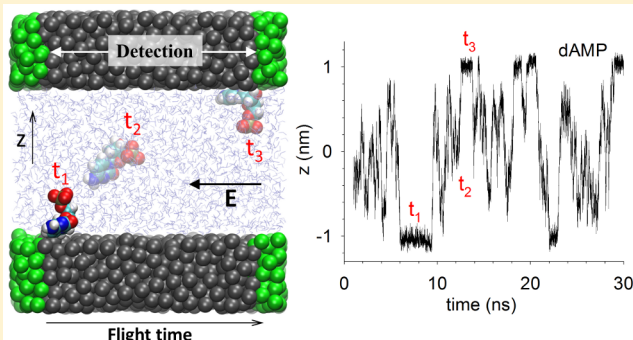
<sup>§</sup>Department of Chemistry, University of North Carolina, Chapel Hill, North Carolina 27599, United States

<sup>||</sup>Department of Biomedical Engineering, University of North Carolina, Chapel Hill, North Carolina 27599, United States

<sup>⊥</sup>Department of Biomedical Engineering, North Carolina State University, Raleigh, North Carolina 27695, United States

## Supporting Information

**ABSTRACT:** There is potential for flight time based DNA sequencing involving disassembly into individual nucleotides which would pass through a nanochannel with two or more detectors. We performed molecular dynamics simulations of electrophoretic motion of single DNA nucleotides through 3 nm wide hydrophobic slits with both smooth and rough walls. The electric field ( $E$ ) varied from 0.0 to 0.6 V/nm. The nucleotides adsorb and desorb from walls multiple times during their transit through the slit. The nucleotide–wall interactions differed due to nucleotide hydrophobicities and wall roughness which determined duration and frequency of nucleotide absorptions and their velocities while adsorbed. Transient association of nucleotides with one, two, or three sodium ions occurred, but the mean association numbers (ANs) were weak functions of nucleotide type. Nucleotide–wall interactions contributed more to separation of nucleotide flight time distributions than ion association and thus indicate that nucleotide–wall interactions play a defining role in successfully discriminating between nucleotides on the basis of their flight times through nanochannels/slits. With smooth walls, smaller nucleotides moved faster, but with rough walls larger nucleotides moved faster due to fewer favorable wall adsorption sites. This indicates that roughness, or surface patterning, might be exploited to achieve better time-of-flight based discrimination between nucleotides.



## INTRODUCTION

Automated DNA sequencing has attracted significant interest since the Human Genome Project began. A major goal is to develop a high-throughput and low-cost method to identify each DNA nucleotide in the correct sequence as it passes a sensor(s). There are three major sequencing approaches of this type under consideration. In some of these approaches intact DNA strands are used,<sup>1</sup> and in others individual nucleotides are first cleaved sequentially from DNA by an exonuclease.<sup>2,3</sup> The first approach involves modification of the nucleotides, and optical detection methods can be used. In the second approach, a DNA strand or single nucleotides from a disassembled strand are passed through a nanopore, and the identity of each nucleotide is determined as it passes.<sup>4–8</sup> The final approach involves passing single nucleotides from disassembled strands through a nanochannel containing multiple detectors. In this approach the flight times of the nucleotides between detectors are used to identify them.<sup>9</sup>

There are also several methods of detection under consideration for use with the above approaches. In optical

methods, fluorescence is used.<sup>10</sup> If an electric field is used to drive DNA or nucleotides through a nanopore, a current associated with the flow of other ions through the pore exists. Part of this current is blocked when a nucleotide is in the pore,<sup>11,12</sup> and the magnitude of the blockage depends upon the nucleotide type. Electrodes might be placed in a nanopore to measure the transverse conductance<sup>10,13–19</sup> or transverse differential conductance<sup>20</sup> associated with each nucleotide as it passes. Sequence specific hysteresis effects were observed when using an ac field with a nanopore.<sup>21</sup> Graphene nanoribbons have been used with nanopores since the currents induced in the nanoribbons from their interaction with each passing nucleotide are orders of magnitude higher than ion blockage currents.<sup>22–25</sup> For flight time based sequencing, the detectors will likely have to involve a restriction similar to a nanopore. In fact, two nanopore systems have been used to

Received: March 23, 2015

Revised: August 3, 2015

Published: August 3, 2015



measure the mobility of DNA<sup>26</sup> molecules and to analyze virus capsids.<sup>27,28</sup> The detection method will also likely be similar to those being considered for the nanopore based methods. The difference is that, in the flight time based method, only the presence of a nucleotide needs to be detected in the electrical signal, not necessarily its identity. Therefore, a noisier signal can be tolerated. Of course a correlation of the electrical signal signature itself with the nucleotide identity could be used as a second level identification basis to increase its fidelity if the signal-to-noise ratio permits.

Optical methods rely on fluorescent labeling to distinguish the nucleotides. Color discrimination has been used to distinguish each nucleotide of an enzymatically disassembled DNA strand with fluorescently labeled nucleotides.<sup>29–31</sup> In another method, each nucleotide is substituted with a unique group of 16 nucleotides, and then each of these oligonucleotides are hybridized to a fluorescently labeled strand; finally, a nanopore is used to remove the fluorescent strand and detect the oligonucleotide type and therefore the identity of the original nucleotide.<sup>10,32</sup> A third method follows the incorporation of fluorescently labeled nucleotide triphosphates as they are added to a growing DNA strand by polymerases.<sup>33</sup>

In nanopore based sequencing methods, the nanopores act to help constrain the configurations of DNA, as the housing for electrodes, or as a constriction to create a blockage in ion current. The reliability and cost for the manufacturing of devices containing nanopores will play an important role in whether these types of DNA sequencing will be successful. Nanopores may be biological or synthetic. Biological pores include the membrane proteins  $\alpha$ -hemolysin<sup>2,11,12,34–37</sup> or porin A.<sup>38</sup> Pores composed of synthetic DNA nanostructures<sup>39,40</sup> or carbon nanotubes<sup>41</sup> spanning a lipid bilayer have been studied. Synthetic pores constructed in silicon nitride<sup>11,42,43</sup> or hafnium oxide,<sup>44</sup> or in 2D materials such as boron nitride,<sup>45,46</sup> graphene,<sup>47–53</sup> or molybdenum sulfide<sup>54</sup> provide additional flexibility including the ability to adjust the pore size and chemically modify the nanopore surfaces or entrap other structures such as synthetic DNA nanostructures<sup>40</sup> within them, and improved mechanical stability compared to membrane-bound systems.

In this research we focus on the flight time based approach for DNA sequencing which involves sequential, enzymatic DNA disassembly into single nucleotides. These nucleotides are driven through a nanochannel with detectors placed at multiple locations. The enzymes used would be  $\lambda$ -exonucleases covalently attached to pillars.  $\lambda$ -Exonucleases have been attached to poly(methyl methacrylate) (PMMA) pillars, and the activity of the attached enzymes was slightly higher than for free enzymes.<sup>55</sup>  $\lambda$ -Exonucleases disassemble one strand of double stranded DNA into single nucleotides with phosphate groups on their 5' ends, deoxynucleotide 5'-monophosphates (dNMPs). The identity of each different type of dNMP, deoxyadenosine 5'-monophosphate (dAMP), deoxycytidine 5'-monophosphate (dCMP), deoxyguanosine 5'-monophosphate (dGMP), deoxythymidine 5'-monophosphate (dTTP), and the epigenetically modified dNMP deoxy-5-methylcytidine 5'-monophosphate (dMCMP), is determined by using the time(s) taken for it to travel between the different detectors (flight time(s) or time(s)-of-flight) as well as the detector signals themselves. The flight times have a specific distribution for each type of dNMP.

The flight time based approach to sequencing has advantages and disadvantages. The main advantage of this method is that

the detectors only need to determine the presence of a dNMP rather than its identity, as mentioned previously making the method less susceptible to noise. The problem of trying to distinguish closely spaced nucleotides in intact DNA does not exist when the DNA is disassembled. The complication of having to introduce immobilized  $\lambda$ -exonuclease enzymes into the system is one of the disadvantages. The use of free dNMPs instead of intact DNA allows for the possibility of misordering due to one dNMP overtaking another one. This can be minimized by changing the magnitude of the driving force or the rate at which the enzyme disassembles the DNA by altering solution conditions such as temperature and pH. Another issue is that diffusion broadens the flight time distributions leading to longer channel lengths and analysis times per dNMP.<sup>9</sup> To reduce this, it is desirable for the magnitude of the driving force to be as large as is practical. If the nucleotide–wall interactions are relied upon to separate the flight time distributions, then the channels should be as narrow as possible so that the dNMPs are in contact with them for a large fraction of the time. The channel walls should also be as homogeneous as possible both chemically and physically since heterogeneities will lead to varying dNMP–wall adsorption energies and broadening of the flight time distributions. The adsorption energies should also be small enough that the dNMPs do not become stuck on the walls for long periods of time since that could lead to misordering. If the interaction of dNMPs with the wall do not result in misordering, they can contribute positively to the discrimination between different dNMPs if the nature and strength of the interaction with the nanochannel walls varies between different dNMPs (e.g., see ref 9).

In this study, using all-atom, explicit solvent, molecular dynamics (MD) simulations, we investigated the electrophoretically driven transport of the four major DNA nucleotide monophosphates or dNMPs (dAMP, dCMP, dGMP, and dTTP) through nanoslits composed of disordered carbon atoms. The main goals include development of fundamental understanding of the mechanism of the dNMP transport and assessment of the likelihood of this type of hydrophobic surface, with no specific dNMP–surface interactions, being suitable for discriminating the flight time distributions of the different types of dNMPs and therefore being useful for flight time based DNA sequencing. The variables considered were the electric field strength and wall roughness.

Various factors influencing the transport of the dNMPs through nanoslits were examined. The strength of the interaction of the dNMPs with the slit walls and their adsorption and desorption behavior is an important factor determining the channel length required to distinguish the flight time distributions of the four dNMP types. Association of counterions with the phosphate group of the dNMPs can lead to a significant change in dNMP velocity along a channel. An understanding of these factors can provide guidance for the design of nanochannel surfaces.

## METHODOLOGY

The simulation system consisted of a dNMP and sodium chloride in water confined between two slit walls. Periodic boundary conditions were used in the directions tangential to the walls. The wall slabs had dimensions of  $5 \times 5 \text{ nm}^2$  in the slit plane. Smooth wall slabs had a depth of 1.2 nm (see Figure 1).

For smooth walls, the atoms in the slit walls were placed outside two planes parallel to the  $xy$  plane, located at  $z = \pm h_{\text{slit}}/2$  nm. The centers of the wall atoms were located at  $z \leq -h_{\text{slit}}/2$

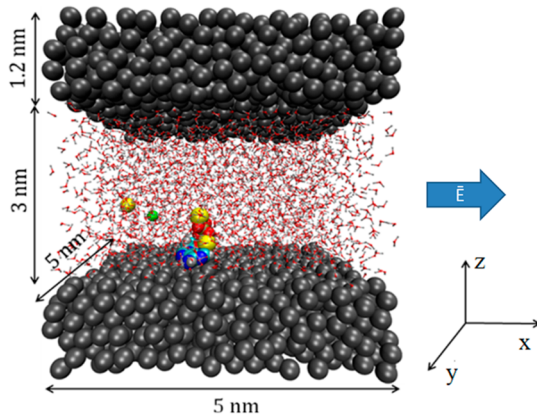


**Figure 1.** Simulation system with smooth walls. Wall atoms (gray), sodium ions (yellow), chloride ion (green), and dNMP atoms are represented as large spheres. The water molecules are in a ball and stick representation. The electric field was applied in the positive  $x$  direction which caused the dNMP to move in the negative  $x$  direction on average.

nm and  $z \geq h_{\text{slit}}/2$  nm. Slit walls were composed of atoms with Lennard-Jones 12-6 parameters for a carbonyl carbon atom ( $\epsilon_{\text{carbon-carbon}} = 0.11$  kcal/mol,  $\sigma_{\text{carbon-carbon}} = 0.4/2^{1/6}$  nm). The mass of the wall atoms was increased from 12.011 to 14.30226 amu, which is the average mass of the atoms in a united atom (no hydrogen atoms, but increased mass of atoms that would have hydrogen atoms bonded to them) representation of PMMA. The details on constructing the smooth slit walls are given in our previous work.<sup>9</sup>

The slit width of 3.0 nm was chosen to maximize the time of contact of the dNMPs with the slit walls while still having bulk solvent near the slit center plane. Real channels with dimensions smaller than 5.0 nm have been fabricated.<sup>56</sup> Note that small, hydrophobic nanoscale geometries are not practical due to the difficulty for aqueous solvent to enter them. The nature of the slit walls was chosen for simplicity in our initial studies. Future work will focus on more realistic walls composed of PMMA or modified PMMA with some of those walls having charged groups which could be important in terms of dNMP–wall interactions as well as for electro-osmotic flow. The description of the construction of the rough walls is somewhat involved and is therefore found in the Supporting Information. There were 10 slits with an average RMS roughness of 2.2708 nm constructed and used in the rough wall simulations. The spacing between the slit walls was chosen so that the volume accessible by the dNMPs was approximately the same as in the smooth wall cases.

Once the walls were constructed, dNMPs were placed between the slit walls and water, and ions were added using the Visual Molecular Dynamics (VMD) software.<sup>57</sup> Constant pressure simulations could not be performed in LAMMPS using long-range electrostatics in the slab geometry, so the amount of water was determined by trial and error and interpolation. The Solvate function in VMD was used to add water. The Solvate settings used were the following: boundary = 2.4,  $x$  and  $y$  bounds =  $\pm 25.65$  Å,  $z$  bounds =  $\pm 15$  Å for the smooth wall cases, and boundary = 2.4,  $x$  and  $y$  bounds =  $\pm 25.44$  Å,  $z$  bounds sufficient to be at or beyond the rough part of the slabs for the rough wall cases. These settings gave a reasonable equilibrium bulk density of water for the model that was used (1.015 g/cm<sup>3</sup> at the center of the slit) in equilibrium

simulations containing only water and the slit walls. For the trial and error density calculation for the rough wall case, the slit with walls with an RMS roughness of 2.2747 nm was used. After using Solvate, some water molecules were replaced with two sodium ions to neutralize the system, and an extra sodium and chloride ion using the Autoionize function in VMD. Final configurations for the smooth wall cases contained between 2199 and 2233 water molecules. Final configurations for the rough wall cases contained between 2264 and 2356 water molecules. Ion concentrations ( $[\text{Na}^+] + [\text{Cl}^-]$ ) were between 100.7 and 102.3 mM for smooth wall cases and between 95.5 and 99.4 mM for rough wall cases based on bulk water density to estimate the volume of solvent.

The CHARMM27 force field<sup>58</sup> was used for the dNMP and ion parameters. The rigid CHARMM TIP3P model was used for water. dNMPs with the phosphate group on their 5' end can be produced by cutting up double-stranded DNA using a  $\lambda$ -exonuclease enzyme. The  $\lambda$ -exonuclease enzyme that would be used for this would likely have the highest activity near the physiological pH of around 7.4. The  $pK_a$  for the first protonation of the phosphate groups of the dNMPs is around 6.8,<sup>59</sup> so the phosphate groups were simulated as nonprotonated which gave the dNMPs a net charge of  $-2e$  where  $e$  is the electron charge. The CHARMM27 topology file did not contain a terminal segment for DNA with a nonprotonated phosphate on the 5' end. Construction of the required patch for a nonprotonated phosphate on the 5' end was explained in previous work,<sup>9</sup> and the patch was included in the Supporting Information for that work. The chemical structure of the simulated dNMPs is shown in Figure 2.

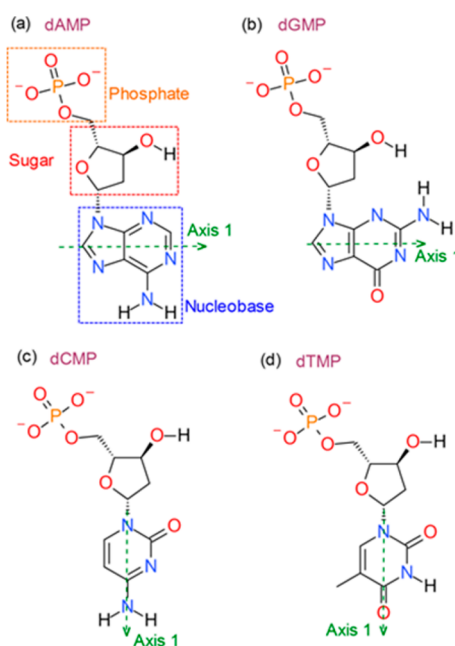


**Figure 2.** Structure of nucleotides with the unprotonated phosphate group attached to the 5' atoms of their sugars. Axis 1 was defined by atoms in the nucleobase rings, and some analysis of nucleobase configuration was based on it. If axis 1 passes through an atom in the picture, then the position of that atom was one of the points used to define the axis. With dAMP and dGMP, the axis passes between two pairs of atoms. The geometric center of the pair furthest from the end of the nucleobase where the sugar is attached was used for the second point needed to define the axis.

Nonbonded interactions were treated as follows. The Lennard-Jones 12-6 interactions were switched to zero between 0.8 and 1.0 nm using the CHARMM switching function. The CHARMM force field uses Lorentz–Berthelot mixing rules to determine Lennard-Jones 12-6 parameters between atoms of different types. The short-range cutoff for electrostatic interactions was 1.0 nm. The 3-D particle–particle particle–mesh (PPPM) method corrected for a slab geometry was used<sup>60</sup> with the minimum accuracy in the PPPM forces set to  $10^{-5}$ . The box length for the PPPM in the nonperiodic direction was 3 times the simulation box length in that direction.

Wall atoms were at a much higher density than Lennard-Jones particles would be at under the simulated conditions. Since a thermostat was applied to the wall atoms (see below), their positions could not be fixed. Therefore, to keep the walls intact, the wall atoms were attached to their initial positions by springs with force constants of  $83\,860\text{ kJ/mol nm}^2$ . This value for the force constants was chosen to minimize expansion of the walls while still being small enough to allow the use of a 2.0 fs time step in the MD integration algorithm.

Since the dNMPs have a net charge, they can be driven electrophoretically. For the nonequilibrium simulations, electric fields with strengths ranging from 0.0144 to 0.6 V/nm were applied to all atoms. The average steady state dNMP velocities in the direction of the applied field ranged from about 0.18 to 31 m/s. Simulation at high velocities relative to velocities typical of nanoscale flows is necessary in MD simulations to obtain statistically meaningful results in the relatively short time that can be simulated, nanoseconds to microseconds.

During nonequilibrium simulations, energy is continuously added to the system so a thermostat was used to remove it. To avoid any artifacts caused by thermostating the flowing solvent and dNMP, only the wall atoms were thermostated at 300 K using a Berendsen thermostat with a time constant of 0.1 ps. The fluid temperatures at steady state were no more than 10 K higher than the temperature of the thermostated walls due to viscous heating of the fluid. Equilibrium simulations were thermostated in the same way as the nonequilibrium simulations.

The following cases were simulated. Simulations with smooth walls were run for all four dNMPs with the electric field strengths of 0.0, 0.0144, and 0.1 V/nm. For the electric fields of 0.0 and 0.0144 V/nm, five simulations with different starting configurations for the wall atoms<sup>9</sup> were run with 70 ns of production time for each mononucleotide; for each of these electric field systems the total simulation time per nucleotide was 350 ns. To better understand the effect of limited MD simulation time on the characteristics of dNMP translocation through nanochannels for the smooth walls systems with 0.1 V/nm electric field, an additional 70 ns of production time was added for each dNMP; the total simulation time per nucleotide for these systems was therefore extended to 700 ns. Additional simulations with smooth walls were run for dTMP only with the electric field strengths of 0.3 and 0.6 V/nm using 5 different wall configurations for each electric field strength and 40 ns of production time per simulation. Finally, nonequilibrium simulations with rough walls were run for all nucleotide types with an electric field of 0.1 V/nm using 10 different wall configurations and with production times per simulation of 40–62 ns. The RMS roughness values of the walls were 1.9799, 2.1131, 2.1967, 2.2085, 2.2747, 2.2926, 2.3326, 2.3412, 2.4411, and 2.5272 nm with an average of 2.2708 nm. The first 10 ns of

each simulation was discarded to allow the simulation to reach a steady state before sampling.

## RESULTS AND DISCUSSION

The primary variables for flight time based sequencing include the rate at which the enzyme disassembles a DNA strand, the nanochannel length, the number of detectors, the nanochannel dimensions, the magnitude and type of the driving force pushing the dNMPs through the nanochannel, and the interactions of the dNMPs with the channel walls and other species in solution. A secondary variable is the redundancy: how many times each DNA sequence is analyzed, either in serial or in parallel. A given identification accuracy can be obtained by modifying both the primary variables and the secondary variable; more redundancy means the time-of-flight distributions in each nanochannel do not have to be as well-separated.

The application relevant goal is to reduce the time required to analyze each dNMP below some acceptable maximum value and to minimize the cost to analyze each dNMP. For a given set of flight time distributions over some length, the following conditions have to be met for sequencing to be successful: (1) The enzyme disassembly rate must be set so that the time between dNMPs being cleaved is at least equal to the time between the upper edge of the flight time distribution over the distance between the first and last detectors for the fastest dNMP type and the lower edge of the flight time distribution over the distance between the first and last detectors for the slowest dNMP type to avoid the problem of misordering caused by dNMPs passing each other in the nanochannel. (2) Either the nanochannel length must be long enough for the flight time distributions to be adequately separated for reliable identification of the dNMPs or the redundancy must be large enough for the chosen nanochannel length to obtain reliable identification of the dNMPs. In addition, the number of detectors should be as large as practical or cost-effective since this additional redundancy improves the ability to identify each dNMP allowing for shorter nanochannel lengths and analysis times.

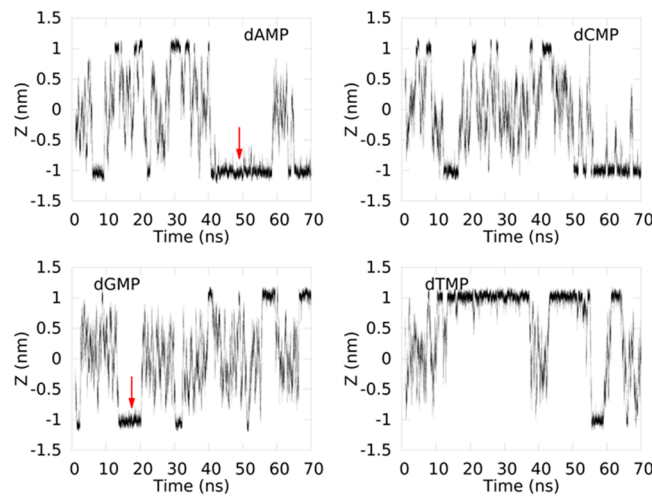
The flight time distributions are determined by the magnitude and type of the driving force, and by the interactions of the dNMPs with the rest of the system. The standard deviations of the flight time distributions decrease with increasing nanochannel length, so assuming the distributions for each type of nucleotide are not exactly the same for a given length, they will eventually not overlap for long enough lengths. To obtain reasonable nanochannel lengths and analysis times, the flight time distributions for a given length need to be sufficiently separated. Since the dNMPs are charged, they can be driven electrophoretically. In that case, each nucleotide will have a different electrophoretic mobility. Unfortunately, the different dNMP types are of similar size and have the same charge, so their mobilities are similar. Relying only on mobility differences would not provide good separation of the flight time distributions. Although the different dNMP types are similar in size, their nucleobase groups are chemically different which allows the interactions of the dNMPs with other parts of the system to be exploited to separate the flight time distributions. This is the factor exploited by chromatography which can be used to separate or analyze different dNMP types from a solution containing multiple types.<sup>61,62</sup> The flight time based approach is essentially a single molecule version of chromatography.

Since this study only involved the motion of dNMPs through a nanoslit and did not involve the exonuclease enzyme or detectors, the factors of interest were the dNMP–wall and dNMP–counterion interactions. Statistics and dynamics of the dNMP adsorption to and desorption from the slit walls were calculated. dNMP orientation during adsorption and desorption; fraction of time adsorbed; frequency of adsorption and desorption events; and the mean times, distances traveled by the dNMPs in the direction of the driving force, and velocities in the direction of the driving force while adsorbed and desorbed were calculated. The mean association numbers of the sodium ions with the dNMP phosphate groups were calculated as well as the characteristic relaxation times for states where 1 or 2 sodium ions were associated with the phosphate group. From the dNMP velocity distributions, the required channel lengths and minimum analysis times per dNMP were estimated. There were two parameters of interest: the strength of the electric field driving the dNMPs and the roughness of the slit walls. Uncertainties were 2 times the standard deviation of the mean unless otherwise indicated. A description of the calculation of uncertainties for all quantities is included in the *Supporting Information*.

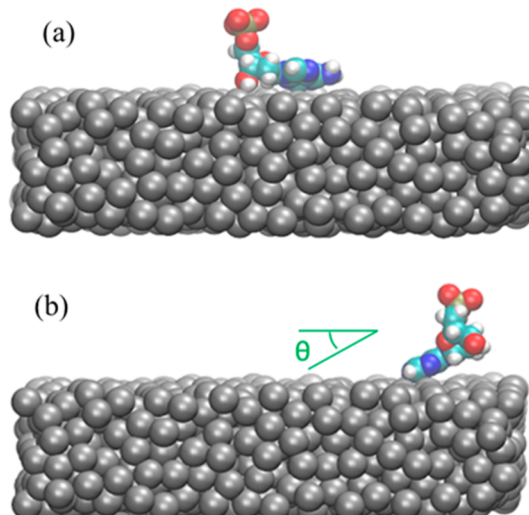
**dNMP Adsorption and Desorption.** In nanoscale geometries, the interaction of the solvent and the solutes in solution with the walls becomes more important since the volume of the solution–wall interfacial region becomes a significant fraction of the total solution volume. As mentioned above in the context of flight time based sequencing, the interaction of dNMPs with the nanochannel walls is important for distinguishing the flight time distributions of the different dNMP types. In nanopore based sequencing, the interaction of DNA or single dNMPs with the nanopore walls could also be important. The effect of binding of DNA to the polymer layer anchored on a nanochannel or directly on the surface of a nanochannel has been examined.<sup>63–65</sup> During the translocation process through nanochannels, DNA is subjected to a series of adsorptions and desorptions to and from the wall surfaces. These transient adsorption events result in an effective mobility decrease. This adsorption and desorption phenomenon is also observed in the electrically facilitated transportation of proteins through large nanopores.<sup>66</sup> Our results presented below show that the dNMPs in our systems also undergo adsorption to, and desorption from, the walls.

Figure 3 depicts the time dependence, over 70 ns, of the dNMP Z-coordinate (wall normal direction) trajectory of the four dNMPs driven by an electric field of 0.1 V/nm. These plots show that all dNMPs adsorb to and desorb from the wall multiple times during the 70 ns trajectories and that the time interval of the adsorption events varies between about 1 and 20 ns. It also shows a clear difference between the trajectories of the four dNMPs as indicated by the frequencies and duration of the adsorption events. Thus, on the basis of the Z coordinate of the center of mass of the dNMPs, a trajectory was decomposed into adsorbed states and desorbed states which alternate with each other. The method of determining these states was described in the Supporting Information of our previous work<sup>9</sup> for the smooth slit walls, and is described in the *Supporting Information* for this paper for the rough slit walls.

In the adsorbed state, the hydrophobic nucleobase parts of the dNMPs tend to sit on the surface while the hydrophilic phosphate group points away from the surface. Figure 4a shows a snapshot of dAMP with its nucleobase fully adsorbed on a wall. The end of the nucleobase furthest from the hydrophilic



**Figure 3.** Position of the center of mass of the dNMPs driven by an electric field of 0.1 V/nm in the wall normal direction ( $Z$ ) over 70 ns. The center of the slit is at  $Z = 0$ . Red arrows in the dAMP and dGMP trajectories indicate examples of periods when the dNMP was adsorbed to a slit wall.



**Figure 4.** Snapshots of dAMP near a wall. (a) The nucleobase and sugar of dAMP are adsorbed. (b) The sugar is detached and the nucleobase is inclined with axis 1 (see Figure 2) forming an angle  $\theta$  with the wall plane during adsorption.

phosphate group was more apt to stick on the hydrophobic wall, and thus, the nucleobases were inclined to the wall surface when they were in the process of adsorbing to or desorbing from the walls as in Figure 4b showing a snapshot of dAMP in the process of being adsorbed to a wall.

For the smooth wall cases the orientation of the dNMP nucleobases relative to the wall surface planes, and relative to the direction of the electric field, were calculated during adsorption and desorption. Specifically, the angles between axis 1 defined in Figure 2 with the wall surface planes and with the electric field direction were calculated. The periods for adsorption were defined to be from midway between the previous desorption instant and an adsorption instant until midway between that adsorption instant and the next desorption instant. The periods for desorption were defined to be from midway between the preceding adsorption instant and a desorption instant until midway between that desorption

instant and the next adsorption instant. Adsorption and desorption instants are at the beginning of an adsorption or desorption period, respectively.

The average angles ( $\theta$ ) of axis 1 (see Figure 2) of the nucleobase parts of the dNMPs with the wall surfaces are plotted in Figure 5 as a function of distance from the nearest

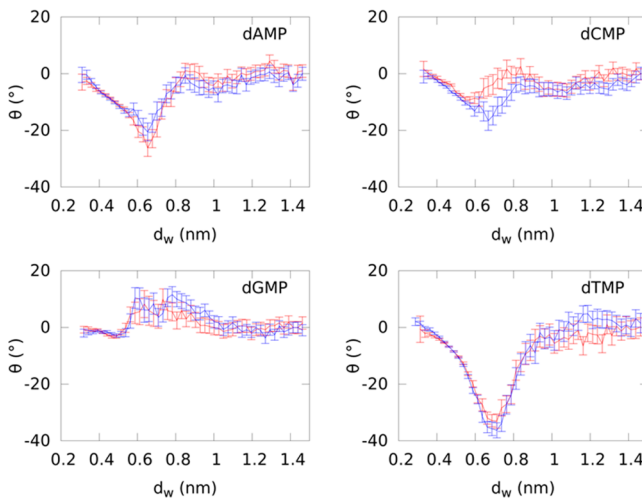


**Figure 5.** Angle between axis 1 (see Figure 2) of the nucleobase and the wall surface as a function of the distance to the wall surface,  $d_w$ , while the dNMP was adsorbing (red) and while the dNMP was desorbing (blue) for the systems with  $E = 0.1$  V/nm.

wall surface ( $d_w$ ) for  $E = 0.1$  V/nm. The behavior was similar for the electric field strengths of 0.0 and 0.0144 V/nm (plots in Supporting Information), indicating that the electric field did not affect the mechanism of adsorption and desorption, at least at the lower field strengths that were studied. Negative values mean that the end of the nucleobase attached to the sugar was further away from the wall than the opposite end; axis 1 pointed toward the wall plane. For  $d_w > 0.9$  nm, the average angles for the four dNMPs were nearly zero. For  $d_w < 0.9$  nm, dAMP, dCMP, and dTMP had minima in  $\theta$  for both adsorption and desorption, indicating that the sugar adsorbed after the nucleobase and desorbed before the nucleobase. The magnitude of the minima of  $\theta$  followed the order dCMP < dAMP < dTMP, which was consistent with the order of hydrophobicity of their nucleobases.<sup>67,68</sup> For  $d_w < 0.9$  nm, dGMP had a maximum in  $\theta$  for both adsorption and desorption, indicating that the sugar adsorbed before the nucleobase and desorbed after the nucleobase. The different behavior of dGMP was likely because its nucleobase was the least hydrophobic.<sup>67,68</sup> The adsorption and desorption curves for each type of dNMP were similar to each other which indicated that adsorption and desorption occurred in a similar way.

The average angles ( $\psi$ ) of axis 1 with the electric field direction were also calculated for  $E = 0.1$  V/nm and lower. Far from the wall for  $E = 0.1$  V/nm, the average angles deviated by about 5–30° from the 90° they would be if the orientation was random. This deviation depended on the type of dNMP, with the smaller pyrimidine based dNMPs showing more deviation. This result was not deemed to be crucial to the discussion of the other results, so plots and a discussion of them were placed in the Supporting Information.

Fractions of the total time during which the dNMPs were adsorbed to the slit walls ( $f_{t,ads}$ ) are shown in Figure 6a as

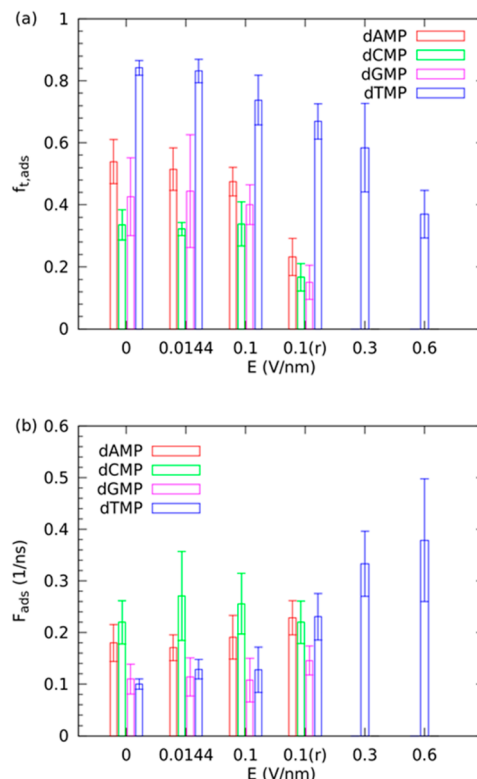


**Figure 6.** Statistics for the dNMPs while adsorbed. (a) Fractions of the total time that the dNMPs were adsorbed to the slit walls. (b) The frequency of adsorption events.

functions of the electric field strength for smooth walls. Figure 6a also includes one rough wall case designated by 0.1(r) on the electrical field axis scale. The fraction of time adsorbed was larger for the more hydrophobic nucleotides (dAMP and dTMP) and generally decreased with increasing electric field strength. Comparison of the smooth and rough wall cases at  $E = 0.1$  V/nm showed that wall roughness reduced the fraction of the time adsorbed for dAMP, dCMP, and dGMP. However, wall roughness had little effect on  $f_{t,ads}$  for dTMP. As discussed previously, the nucleobase parts of the dNMPs tended to sit almost flat on the wall. When the wall was rough, the nucleobases had fewer locations where that was possible, leading to more frequent desorption and a tendency toward reduced fraction of time adsorbed on the wall. The dTMP nucleobase was the most hydrophobic of the nucleobases. Therefore, even though it desorbed more easily from rough walls compared to smooth walls it still readsorbed relatively quickly. This behavior was reflected in its much higher frequency of adsorption on rough walls compared to smooth walls which is shown in Figure 6b. Thus, dTMP's fraction of time adsorbed was more insensitive to wall roughness than the other dNMPs.

The frequencies of adsorption events ( $F_{ads}$ ) are shown in Figure 6b as functions of electric field strength for smooth walls and for the one rough wall case, 0.1(r). For smooth walls, higher frequency was correlated with a lower fraction of time adsorbed (see Figure 6a); i.e., in a comparison between dNMPs, most of those who spent less time adsorbed also adsorbed more frequently. dGMP was the exception, which had short fractions of time adsorbed and adsorbed least frequently. The adsorption frequency was higher for the rough wall case for the same electric field strength for all dNMPs except dCMP. As

mentioned above, dTMP displayed a significantly higher adsorption frequency when the walls were rough, which nearly overcame its ease in desorbing from the rough walls. So, dTMP displayed the same fraction of time adsorbed irrespective of the wall roughness. The adsorption frequency of dTMP increased significantly with increased electric field strength for  $E > 0.1 \text{ V/nm}$ .

Mean times per adsorption event ( $t_{\text{ads}}$ ) are shown in Figure 7a as functions of electric field strength for smooth walls and for the one rough wall case, 0.1(r). The trends were consistent with those for the fractions of time adsorbed. The mean time per adsorption event generally decreased with increasing

electric field strength, most convincingly so for dTMP and least for dCMP. Adding roughness to the slit walls caused a significant decrease of  $t_{\text{ads}}$  with dTMP displaying the least sensitivity to roughness.

The mean velocities ( $v_{\text{ads}}$ ) of the dNMPs along the direction ( $-x$ ) of the force driving them while adsorbed to the slit walls are shown in Figure 7b as functions of electric field strength for smooth walls and for the one rough wall case, 0.1(r). The velocities of the different dNMPs at a given electric field strength were statistically similar in magnitude. This means that, despite the differences in the dNMP–wall interactions in the wall normal direction,<sup>9</sup> the interactions in the wall tangential directions were statistically similar for all dNMPs. The differences in the dNMP nucleobase sizes and in the mean sodium–dNMP association numbers (discussed later) also affected the velocities, but those effects were small. The velocities naturally increased with increasing electric field strength. The results from the single rough wall case indicated that making the slit walls rough reduces the velocities of the dNMPs while adsorbed by a factor of about 1.5–2.

Mean distances ( $d_{\text{ads}}$ ) traveled by the dNMPs in the direction ( $-x$ ) of the force driving them while adsorbed to the slit walls are shown in Figure 7c as functions of electric field strength for smooth walls and for the one rough wall case, 0.1(r). The effect of the electric field strength on this distance was influenced by the competing effects of the increased dNMP velocity while adsorbed and the decreased time per adsorption event with increased electric field strength. Mean distances per adsorption event of the dNMPs at  $E = 0.1 \text{ V/nm}$  were higher than at  $E = 0.0144 \text{ V/nm}$ . However, the distances at  $E = 0.3 \text{ V/nm}$  and  $0.6 \text{ V/nm}$  were not much larger than at  $E = 0.1 \text{ V/nm}$ ; the increasing dTMP velocity while adsorbed was offset by the decreasing time per adsorption event. As with the time per adsorption event, rough walls decreased  $d_{\text{ads}}$  for dAMP, dCMP, and dGMP by much more than for dTMP.

Mean times per desorption event ( $t_{\text{des}}$ ) are shown in Figure 8a as functions of electric field strength for smooth walls, including one rough wall case, 0.1(r). The mean time per desorption event was modestly affected by changing the electric field strength since it depended on the motion of the dNMPs in the wall normal direction and their adsorption and desorption dynamics, which as mentioned previously were not significantly affected by the electric field strength. Adding roughness to the slit walls also generally had little effect on  $t_{\text{des}}$ . The order for  $t_{\text{des}}$  for nonzero electric field was usually dTMP < dAMP  $\leq$  dCMP < dGMP, which was the reverse of the hydrophobicity order of the nucleobases, G < C < A < T.<sup>67,68</sup> Increased hydrophobicity likely led to a greater capture probability, the probability that a dNMP will adsorb when it comes near a wall instead of bouncing off, and therefore to a lower mean time per desorption event.

The mean velocities ( $v_{\text{des}}$ ) of the dNMPs along the direction ( $-x$ ) of the force driving them while desorbed from the slit walls are shown in Figure 8b as functions of electric field strength for smooth walls and for the one rough wall case, 0.1(r). As expected, the velocities were statistically similar for all the dNMPs at any given electric field strength. Any small differences were due to the differing size of the dNMP nucleobases and the differences in the mean sodium–dNMP association numbers, which are discussed later. The velocities of the dNMPs increased with increased electric field strength, again as expected. The walls had little effect on the dNMPs when they were desorbed, so  $v_{\text{des}}$  values for the rough and

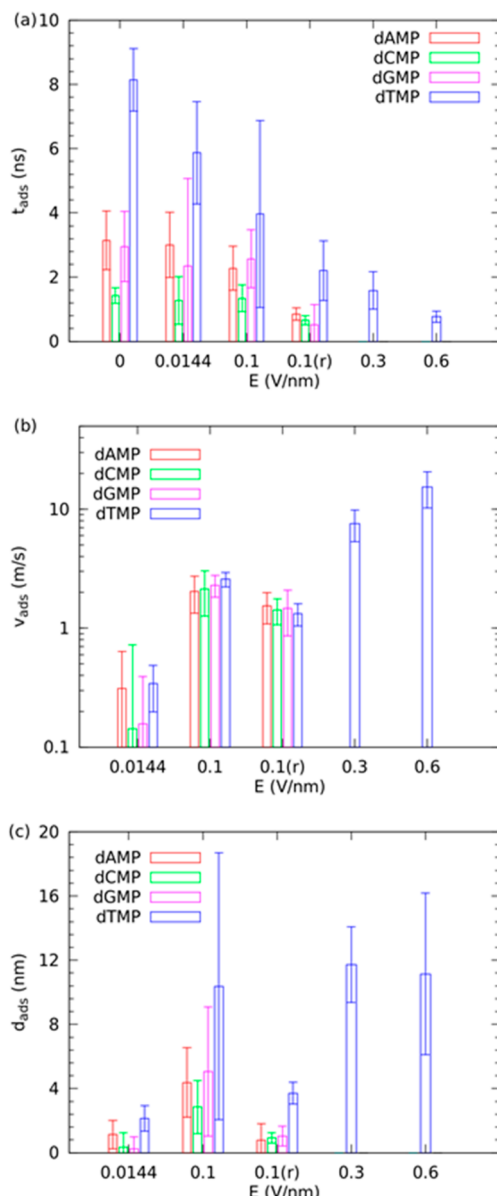


**Figure 7.** Statistical variables for the dNMPs while adsorbed as functions of electric field strength for smooth slit walls and for the one case with rough slit walls designated as 0.1(r). (a) The mean times per adsorption event. (b) Mean velocities of the dNMPs along the direction ( $-x$ ) of the force driving them while adsorbed to the slit walls (vertical axis is logarithmic). (c) Mean distances traveled by the dNMPs along the direction ( $-x$ ) of the force driving them while adsorbed to the slit walls.

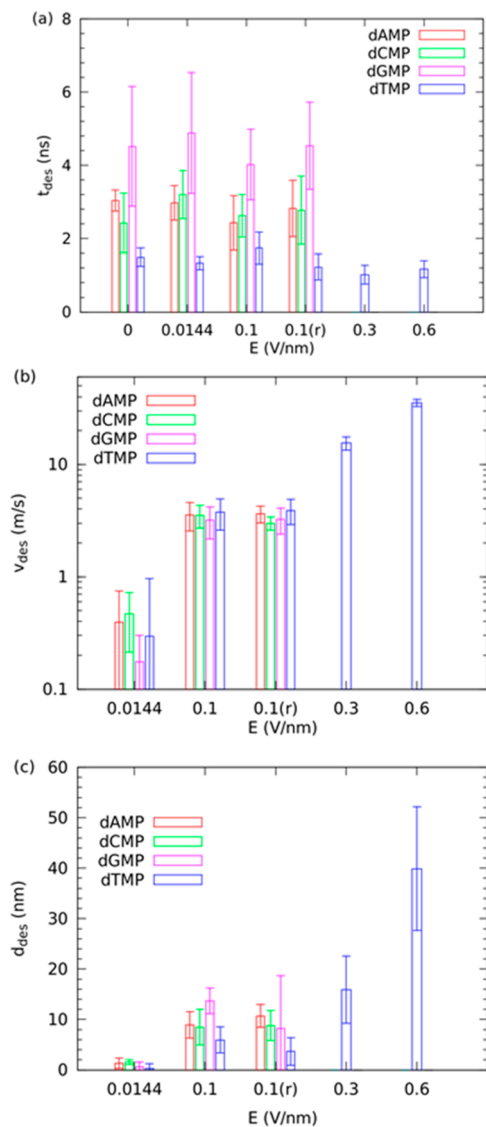


**Figure 8.** Statistical variables for the dNMPs while desorbed as functions of electric field strength for smooth slit walls and for the one case with rough slit walls designated as  $0.1(r)$ . (a) The mean times per desorption event. (b) Mean velocities of the dNMPs along the direction ( $-x$ ) of the force driving them while desorbed from the slit walls (vertical axis is logarithmic). (c) Mean distances traveled by the dNMPs in the direction ( $-x$ ) of the force driving them while desorbed from the slit walls.

smooth walls at  $E = 0.1$  V/nm were statistically the same as expected. The consistency of these results with what is expected based on fundamentals was a good indication that the simulations conducted were trustworthy.

Mean distances ( $d_{des}$ ) traveled by the dNMPs in the direction ( $-x$ ) of the force driving them while desorbed are shown in Figure 8c as functions of electric field strength for smooth walls and for the one rough wall case,  $0.1(r)$ . The distances increased with increasing electric field strength. As with the time per desorption event,  $d_{des}$  was affected by the hydrophobicity of the dNMPs.

**dNMP Phosphate Association with Sodium Ions.** Negatively charged DNA strongly interacts with positively charged counterions which can form a stable layer near DNA in solution and play an important role in altering DNA structure and modulating the interaction between DNA and other

molecules.<sup>69–71</sup> The counterion layer is too stable to be removed by conventional deionization methods. However, recent research found that an electric field can promote the dissociation of the DNA–ion complex during capillary electrophoresis resulting in irregular DNA migration velocity.<sup>72</sup> The interaction of cationic counterions with the dNMPs is important since tightly bound ions can effectively reduce or even reverse the sign of the charge on the nucleic acid–counterion complex which reduces or reverses the sign of the force on the complex due to the electric field. For example, smaller alkali metal cations bind to DNA more strongly:  $\text{Li}^+ > \text{Na}^+ > \text{K}^+$ . Kowalczyk et al.<sup>73</sup> exploited this by using  $\text{Li}^+$  instead of  $\text{Na}^+$  or  $\text{K}^+$  to slow down the motion of single stranded DNA through a nanopore. Indeed, our simulation results for the motion of dNMPs in nanoslits show that transient binding of sodium ions to the dNMPs leads to irregular dNMP velocities.

The phosphate groups of the dNMPs strongly interacted with sodium cations in solution and formed associations with 1, 2, and sometimes 3 sodium ions. This strong association is shown in Figure 9, which is a plot of the radial distribution

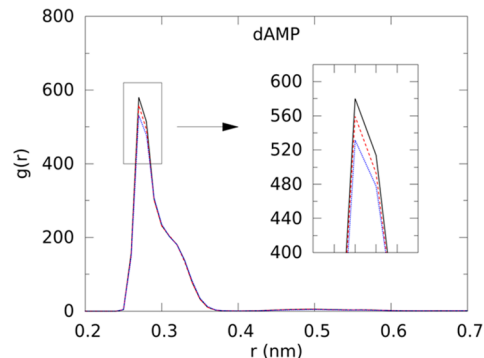


**Figure 9.** Radial distribution functions between the sodium cations and the phosphorus atom in the phosphate group of dAMP. The abscissa  $r$  is the distance between the phosphorus atom and a sodium cation. Black solid lines, red dashed lines, and blue dotted lines are, respectively, for the electric fields of 0.0, 0.0144, and 0.1 V/nm.

function,  $g(r)$ , between the sodium cations and the phosphorus atom on the phosphate group of dAMP. The four dNMPs had similar distribution curves, indicating that their different nucleobase parts had little effect on the association (the plots for the other dNMPs are in the Supporting Information). All distributions had major peaks with magnitudes between about 415 and 610, meaning that a very stable  $\text{Na}^+$  shell was formed around the phosphate group. All the major peaks occurred at around  $r = 0.27$  nm. There are small secondary peaks around  $r = 0.5$  nm. The major peak widths were not affected by the electric field at all, but the peak height generally decreased with increasing electric field strength, and thus, the peaks were flattened slightly.

To capture the entire major peak but not the secondary peak of  $g(r)$ , the cutoff distance to decide whether a  $\text{Na}^+$  ion was associated with the phosphate group was chosen to be 0.4 nm. Use of a single cutoff distance led to some very short association events because a sodium ion crossed outside the cutoff distance and then right back inside it, or the reverse. This was avoided by only counting association states which lasted longer than a minimum time of 0.4 ns. This time removed the noise due to the single cutoff distance, yet was still less than the mean time after a sodium dissociated from a dNMP until it

passed the dNMP again through the periodic boundaries for electric field strengths of 0.0144 and 0.1 V/nm; it was unlikely that the use of this minimum time caused two association events to be counted as one. Use of a minimum time of 0.4 ns was equivalent to doing a 0.4 ns moving average on the association number trajectory followed by rounding to the nearest integer. Application of the minimum time had little effect on the mean association number, but affected dynamical quantities such as the mean relaxation time for association.

The association number versus time for a 70 ns segment of the trajectory for each dNMP with  $E = 0.1$  V/nm is shown in Figure 10. The coordinates of the center of mass of the dNMPs

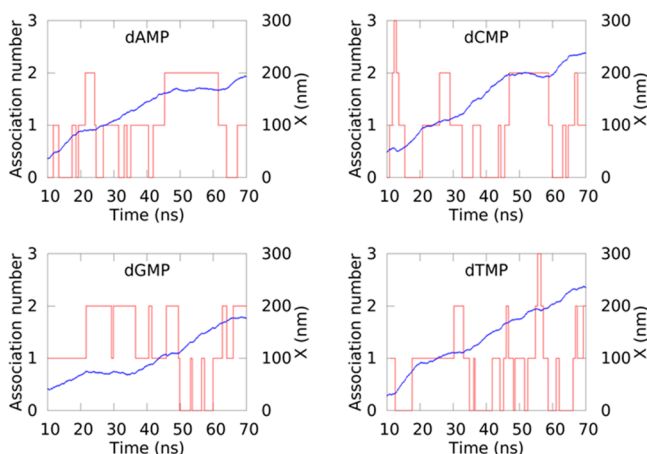


**Figure 10.** Association number of sodium cations with the dNMP phosphorus atom (red), and the  $-x$  coordinate (direction of the driving force) of the center of mass of dNMPs (blue) as a function of time over a 70 ns segment of the trajectory. The electric field strength was 0.1 V/nm.

in the direction of the driving force ( $-x$ ) are also plotted in the same figures. The figures show that the traveling velocity of dNMPs (i.e., the slope of  $x$ -coordinate versus time curve) was strongly influenced by the association formed between  $\text{Na}^+$  and the dNMPs. Take dGMP for example and compare three time periods: from 10 to 20 ns the  $x$  coordinate increased linearly with time, and the association number was 1; from 20 to 36 ns the  $x$  coordinate remained nearly the same, and the association number was 2; from 50 to 60 ns the  $x$  coordinate increased in time with a steeper slope than the first time period, and the association number was generally 0, occasionally 1. The dNMPs were driven by the electric field so the driving force was proportional to the net charge on them. With no  $\text{Na}^+$  bound, the net charge of the phosphate group was  $-2e$ . With one  $\text{Na}^+$  ion bound to the phosphate group, the net charge of the aggregate was  $-1e$ , and thus the driving force was reduced to half. If two  $\text{Na}^+$  ions were associated simultaneously, the aggregate was electrically neutral, and the driving force became zero; thus, the  $x$  coordinate remained the same in that time period.

Despite the effect of the individual sodium–phosphate association events on the dNMP velocity, overall the association did not have a significant effect since the mean association numbers were not affected much by the electric field strength or the roughness of the walls as shown in Figure 11. Even after averaging over all dNMPs for each case, the error bars still overlapped for all cases; none of the differences were significant. There appeared to be a small decrease in the

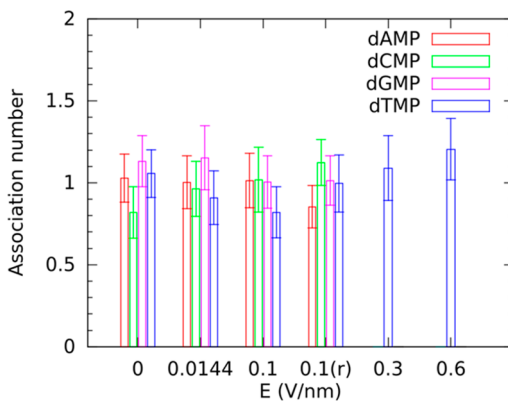


**Figure 11.** Mean association numbers for the dNMPs.

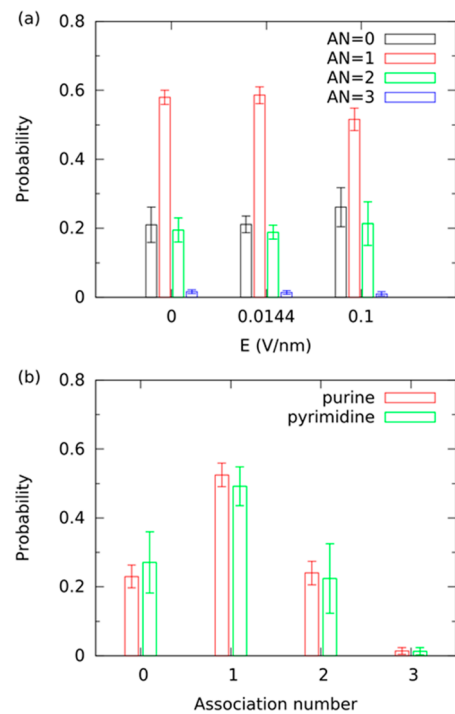
association number-averaged over all dNMPs with increased electric field strength from 0.0 to 0.1 V/nm. This was to be expected since the electric field pulled the sodium ions and dNMPs in opposite directions which was not favorable for association. The association numbers for dTMP at electric fields  $E = 0.3$  and  $0.6$  V/nm appeared to be slightly higher than that for  $E = 0.1$  V/nm and were increasing with increased electric field strength, but this could be an artifact of the periodic boundary condition; once a sodium ion dissociated from a dNMP, it did not take long before they passed each other again since they were moving at relatively high velocities in opposite directions which gave them little time to diffuse out of the path of each other and possibly increased the probability of reassociation. Therefore, this variation with increasing electrical field was deemed insignificant.

Figure 12a shows the distribution of the  $\text{Na}^+$ –P association numbers (ANs) averaged over all four dNMPs for  $E = 0.0$ , 0.0144, and 0.1 V/nm with smooth walls. The rough wall case with  $E = 0.1$  V/nm is nearly identical to the smooth wall case with  $E = 0.1$  V/nm, so the results for the rough wall are not shown. For all cases the order of the probabilities,  $P[\cdot]$ , was  $P[\text{AN} = 1] > P[\text{AN} = 0] > P[\text{AN} = 2] > P[\text{AN} = 3]$ .  $P[\text{AN} = 3]$  was much lower than the other three states and did not have a significant influence on the traveling velocity of the dNMPs.  $P[\text{AN} = 0]$  increased slightly, and  $P[\text{AN} = 1]$  decreased slightly with increased  $E$  which led to the overall decrease in association number with increased  $E$ .

Figure 12b shows the distribution of the  $\text{Na}^+$ –P association numbers averaged over the dNMPs with purine and pyrimidine nucleobases in the case of smooth walls with  $E = 0.1$  V/nm. The dNMPs with pyrimidine nucleobases (dCMP and dTMP) had a higher  $P[\text{AN} = 0]$  and lower  $P[\text{AN} = 1]$  and  $P[\text{AN} = 2]$  compared to the dNMPs with purine nucleobases (dAMP and dGMP) which led to the overall higher association number for dAMP and dGMP which can also be seen in Figure 11. Other cases showed similar behavior.

The relaxation times for the association were estimated by integration of an aggregate existence autocorrelation function (AEACF) which is a generalization of the dimer existence autocorrelation function (Dacf) described by Brehm and Kirchner.<sup>74</sup> Once an AEACF was obtained it was fit to a function which was integrated from time 0 to infinity to estimate a relaxation time. The details of the AEACF and relaxation time calculation are included in the Supporting Information, as well as a plot of the AEACF curves for one case.

Figure 13a shows the relaxation times for an association number of 1. The relaxation time generally decreased with



**Figure 12.** Distribution of the association numbers for (a) the average over all of the dNMPs for the smooth wall cases with different electric fields, and for (b) the averages over the dNMPs with purine bases (dCMP and dTMP) and over the dNMPs with pyrimidine bases (dAMP and dTMP) with smooth walls and  $E = 0.1 \text{ V/nm}$ .

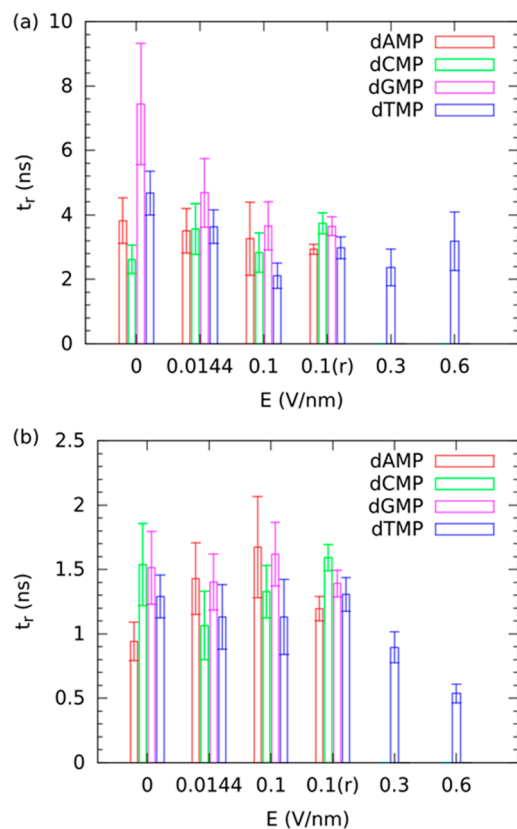


**Figure 13.** Mean relaxation times for a Na<sup>+</sup>–P association number of (a) 1 and (b) 2.

increasing  $E$  because the electric field tended to pull the oppositely charged dNMPs and sodium ions apart. The rough wall case was similar to the smooth wall case at  $E = 0.1 \text{ V/nm}$  except with regards to dTMP. However, there may be a bias in the value for dTMP with smooth walls and  $E = 0.1 \text{ V/nm}$  since the value for dTMP was significantly smaller than that for the other dNMPs only in that case. Figure 13b shows the relaxation times for an association number of 2 which were roughly 2–6 times smaller than for an association number of 1. There was not much difference in the relaxation times for  $E = 0.1 \text{ V/nm}$  and lower for both the rough and smooth walls. The relaxation time decreased for  $E = 0.3$  and  $0.6 \text{ V/nm}$ . The reason for this behavior is unknown, but may have been due to the additional effect of the repulsion between the two sodium ions. The repulsive forces may have been dominant compared to the forces due to the electric field pulling the sodium ions and dNMPs apart at lower electric field strengths, but the forces due to the electric field may have become significant at higher electric field strengths which then led to decreased relaxation times with increased field strength. The sodium ion repulsion may have also led to the decreased relaxation times for an association number of 2 relative to an association number of 1.

**dNMP Velocities.** The mean velocities of the dNMPs gave an indication of how well-separated the flight time distributions would be. The mean velocities of the dNMPs in the nanoslit as a function of electric field strength and wall roughness are shown in Figure 14. At the lowest electric field of  $E = 0.0144$

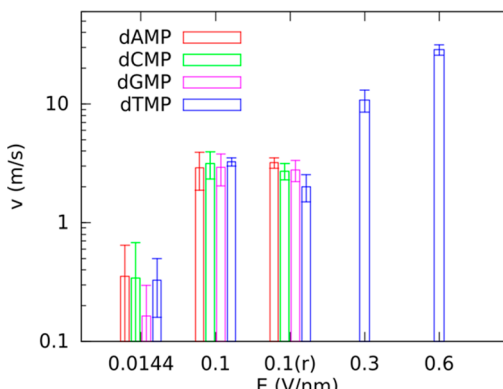


**Figure 14.** Average overall velocities of the dNMPs. Note that the vertical axis is logarithmic.

V/nm, the velocities of dNMPs were nearly equal except for dGMP although the dGMP velocity was still within the uncertainties of the other velocities. For dTMP, four different electric field strengths were used, and the results showed that the velocities increased with electric field strength. The relationship between the average velocity and electric field was not linear, although the driving force on the dNMPs was linearly proportional to electric field. As discussed above, both adsorption to the walls and association between phosphate group and Na<sup>+</sup> ions also affected the traveling velocity of dNMPs. The superlinear increase in the velocity with increasing electric field strength was primarily due to reduction in the fraction of time adsorbed (see Figure 6a). A lower fraction of time adsorbed resulted in a larger velocity since the dNMP was slowed down less due to contact with the walls.

The large uncertainties in the velocities arose for several reasons. The first is that the velocities were much smaller than the thermal velocities especially for the lower electric fields.

Simulation times for the smallest electric field would have to be much longer to reduce the uncertainties to the same relative uncertainty of around 10% or less obtained for the larger electric fields. A second factor contributing to the variability in the velocities was the variability in the time of each association event between the dNMP phosphate group and  $\text{Na}^+$  cations. From Figure 10 it can be seen that the time of one association event ranged from less than 1 to 20 ns. The variability in the adsorption times and in the velocity while adsorbed due to the heterogeneity of the wall surface also contributed to variability in the velocities. The last two factors could also lead to biases as well if there were not enough association events or not enough adsorption events observed in the simulations. Of particular concern were that there were only a limited number of time periods during which the association number was equal to 2, and that especially for dTMP there were only a limited number of adsorption events.

**Distance to Separate the dNMPs and Analysis of the Time-of-Flight per dNMP.** The distributions of dNMP velocities, and therefore the flight times, cannot be separated over the distances traveled by the dNMPs in a few hundred nanoseconds typical for an MD simulation study. However, the results from the MD simulations were extrapolated to much longer times to estimate the minimum required channel length for dNMP separation. The procedure used to extrapolate the time-of-flight distributions over a distance on the order of a few nanometers or tens of nanometers, which are obtained from the MD simulations, to distances of the order of microns or hundreds of microns was presented in detail in our previous work.<sup>9</sup> Following this extrapolation procedure, with some minor modifications outlined below, the simulation time that would be required to separate the distributions to a desired accuracy and therefore the distances traveled by the dNMPs during that time were calculated for each pair of dNMP types. The maximum of those distances was the required channel length. The minimum required analysis times per dNMP were estimated from the width of all of the distributions of the flight times over the required channel length: the distance between the lower edge of the distribution with the shortest flight times and the upper edge of the distribution with the longest flight times. These edges were determined by the accuracy required. The reason that this determined the minimum analysis time is that if a dNMP with the longest flight times passed through the channel followed by one with the shortest flight times, it could not be allowed to pass the previous dNMP; the distributions of the times when the two dNMPs pass the last sensor measured from the beginning of the analysis must be sufficiently separated.

In our previous work, focused on body force driven flow of dNMPs in the nanochannels,<sup>9</sup> the required channel length to achieve reliable separation of the time-of-flight distributions of the dNMPs was calculated from the distributions of the times-of-flight over 0.5 nm segments. These times-of-flight were calculated for each simulation trajectory by starting from the first time step in the trajectory after equilibration, calculating the first time that a dNMP had advanced 0.5 nm beyond its initial position in the direction of the driving force, then repeating the process starting from the next time step in the trajectory after the end of the previous 0.5 nm segment until the end of the trajectory was reached. However, it was just as valid to start at the second, third, etc., time steps after equilibration. This would lead to different sets of times-of-flight and different estimates of the required channel length. In

addition, using only the single sets of flight times determined from the simulation did not lead to the best estimates of the distributions that would be obtained if in fact the simulations could have been extended until the actual distributions no longer overlapped. To fix the problems mentioned above, some modifications to the calculation methodology were made. The distributions of the simulation mean dNMP velocities estimated using the moving block bootstrap method<sup>75</sup> were used instead of the time-of-flight distributions. Since the distributions of the mean velocities were nearly normal, a multiple of the standard deviation could be used as an estimate of the distribution widths instead of the distance between where the cumulative distribution function was equal to  $(1 - \text{separation efficiency})/2$  and  $(1 + \text{separation efficiency})/2$ . The details of the calculations are included in the Supporting Information.

Table 1 shows the required distances for separation of all pairs of dNMP mean velocity distributions to three standard

**Table 1. Required Distances ( $\mu\text{m}$ ) to Separate the Time-of-Flight Distributions of the dNMP Pairs to Three Standard Deviations from the Means of the Distributions for Smooth Walls with  $E = 0.1 \text{ V/nm}$  and  $E = 0.0144 \text{ V/nm}$ , and Rough Walls with  $E = 0.1 \text{ V/nm}$ <sup>a</sup>**

	dAMP	dCMP	dGMP	dTMP
<i>E = 0.0144 V/nm (smooth), 350 ns</i>				
dAMP		<b>165.8</b>	1.2	0.2
dCMP	<b>165.8</b>		1.3	52.2
dGMP	1.2	1.3		0.4
dTMP	0.2	52.2	0.4	
<i>E = 0.1 V/nm (smooth), 350 ns</i>				
dAMP		9.6	<b>105.2</b>	49.1
dCMP	9.6		6.6	26.1
dGMP	<b>105.2</b>	6.6		12.0
dTMP	49.1	26.1	12.0	
<i>E = 0.1 V/nm (smooth), 700 ns</i>				
dAMP		1.3	<b>78.9</b>	12.7
dCMP	1.3		1.5	3.9
dGMP	<b>78.9</b>	1.5		5.6
dTMP	12.7	3.9	5.6	
<i>E = 0.1 V/nm (rough), 350 ns</i>				
dAMP		9.5	16.9	1.4
dCMP	9.5		<b>241.9</b>	3.7
dGMP	16.9	<b>241.9</b>		3.1
dTMP	1.4	3.7	3.1	

<sup>a</sup>The required distances for the smooth walls with  $E = 0.0144 \text{ V/nm}$  and rough wall with  $E = 0.1 \text{ V/nm}$  were obtained from 350 ns MD trajectories. For the case of smooth wall with  $E = 0.1 \text{ V/nm}$  the required distances were obtained from both 350 and 700 ns MD trajectories. The longest distances which are in bold are the minimum required channel lengths.

deviations. The maximum value was considered the minimum required channel length for that level of accuracy. These minimum channel lengths were about 165.8  $\mu\text{m}$  for the smooth wall case with  $E = 0.0144 \text{ V/nm}$  and 350 ns MD trajectories, 105.2 and 78.9  $\mu\text{m}$  for the smooth wall case with  $E = 0.1 \text{ V/nm}$  and 350 and 700 ns MD trajectories, respectively, and 241.9  $\mu\text{m}$  for rough wall case with  $E = 0.1 \text{ V/nm}$  and 350 ns MD trajectories. However, these values were very sensitive to the difference in the estimated overall mean velocities for the pair of dNMPs that determine them. To gain additional insight into this, one block of data (12 ns) was removed from either the

beginning or end of a trajectory in the rough wall case. This was done for all 20 trajectories for dCMP and dGMP since the overlap of their time-of-flight distributions determined the minimum required channel length, leading to 40 data sets that were 12 ns shorter than the full data set from which 40 values of the channel lengths were calculated. The minimum value of these 40 channel lengths was about 75  $\mu\text{m}$ , the maximum value was about 1870  $\mu\text{m}$ , and the median value was about 238  $\mu\text{m}$  (very right skewed). Given this variability, the channel lengths for the different cases were not statistically different.

Since the estimated distribution of the mean velocities could be approximated as normal, the flight time distributions could be easily derived from the velocity distributions. Note that the flight time distributions are not normal and are right skewed (see the *Supporting Information*). The probability density functions for the flight times over the required channel lengths for smooth walls with  $E = 0.0144 \text{ V/nm}$  and  $E = 0.1 \text{ V/nm}$  and rough walls with  $E = 0.1 \text{ V/nm}$  are shown in *Figure 15c* along with the required analysis times per dNMP.

In *Figure 15*, the order of the distributions was different in all three cases. For smooth walls with  $E = 0.1 \text{ V/nm}$ , the dNMPs with the smaller pyrimidine nucleobases (dCMP and dTMP) moved faster than the dNMPs with the larger purine nucleobases (dAMP and dGMP). The order of the flight time distributions,  $\text{dCMP} < \text{dTMP} < \text{dAMP} < \text{dGMP}$ , was also the order of the surface area of the nucleobase part of the dNMPs and the order of the magnitudes of the potential energies between the dNMPs and the wall calculated in previous simulations.<sup>9</sup> This would suggest that the order was simply determined by the interactions of the dNMPs with the walls; those with stronger interactions moved slower when adsorbed which led to slower overall velocities. The trend in the velocities while adsorbed was  $\text{dTMP} > \text{dCMP} \approx \text{dGMP} > \text{dAMP}$  (see *Figure 7b*), but if this simple explanation were true, then the expected order would be  $\text{dCMP} > \text{dTMP} > \text{dAMP} > \text{dGMP}$ . The most important additional factor was the fraction of time adsorbed (see *Figure 6a*) which was related to the hydrophobicity of the dNMP nucleobases.<sup>67,68</sup> dTMP was more hydrophobic than dCMP and spent a much larger fraction of time adsorbed than dCMP, so its overall velocity was lower than that for dCMP even though it moved faster than dCMP while adsorbed. A similar argument holds for dGMP and dAMP; dAMP was more hydrophobic leading to a swapping in the order of their overall velocities compared to their velocities while adsorbed. For smooth walls with  $E = 0.0144 \text{ V/nm}$ , the statistics were too poor and the order of the dNMPs may not be accurate. It may be that dGMP got stopped on the wall more often while adsorbed instead of sliding which could have led to it having much longer flight times than the other dNMPs. However, it is unclear why dAMP would have the shortest flight times. For rough walls with  $E = 0.1 \text{ V/nm}$ , the order of the dNMPs with purine nucleobases and pyrimidine nucleobases was switched compared to the case of smooth walls with  $E = 0.1 \text{ V/nm}$ ; the order of the flight times was  $\text{dAMP} < \text{dGMP} < \text{dCMP} < \text{dTMP}$ . This switching in the order was likely because the change in the fraction of time adsorbed (see *Figure 6a*) decreased more in the rough wall case compared to the smooth wall case for dNMPs with purine nucleobases than for the dNMPs with pyrimidine nucleobases. The likely reason for this was simply geometric; the nucleobases had fewer locations where they could adsorb strongly to the rough walls, and this effect was greater for larger

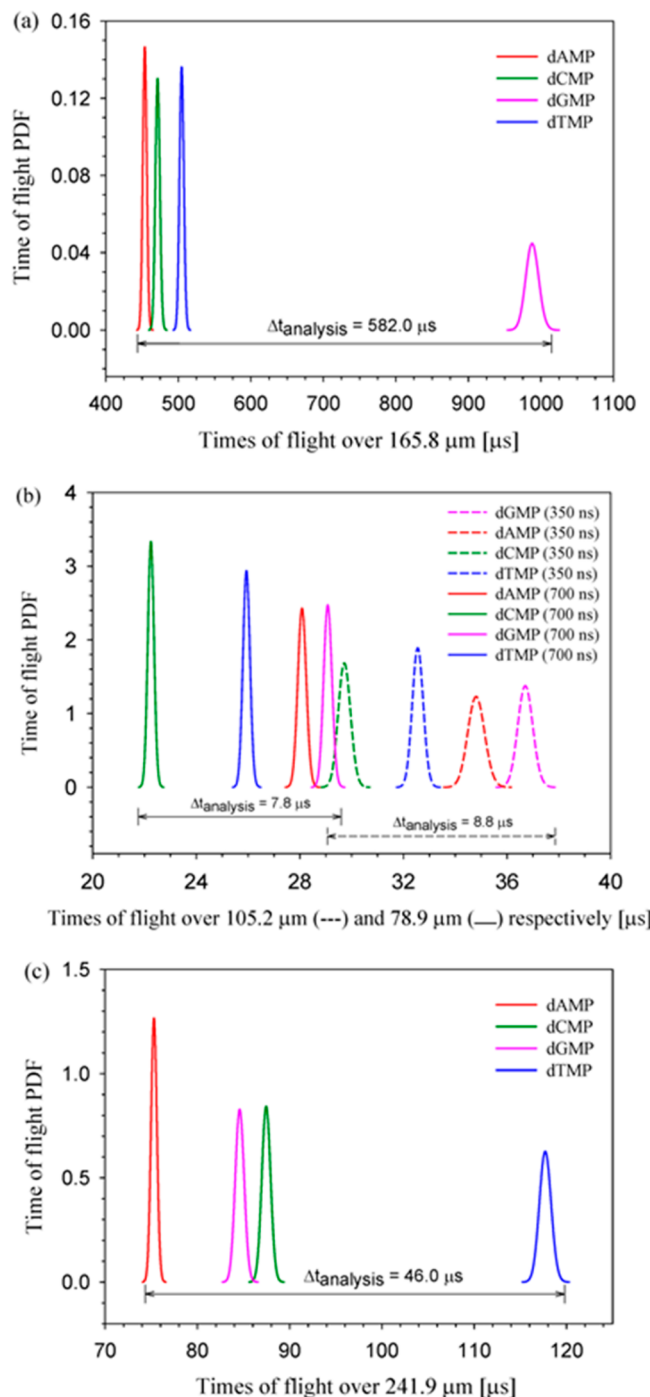


**Figure 15.** Probability density functions (PDFs) of the times of flight for each dNMP for (a)  $E = 0.0144 \text{ V/nm}$  with smooth walls, (b)  $E = 0.1 \text{ V/nm}$  with smooth walls, and (c)  $E = 0.1 \text{ V/nm}$  with rough walls. The PDFs for cases a and c were obtained from 350 ns MD simulation trajectories. For case b, the PDFs obtained from both 350 and 700 ns MD simulation trajectories are shown. The minimum required analysis times per dNMP are also shown on the plots.

nucleobases. This was discussed earlier in the context of the fraction of time adsorbed.

As evident from our studies, when viewed over time- and length-scales typical for MD simulations, the overall characteristics of the translocation of dNMPs through nanochannels have the signature of processes controlled by sequences of infrequent events. It is therefore important to develop an

understanding of the interplay and the role of simulation system characteristics, such as system size and total simulation time, and the various intrinsic quantities, such the duration and frequency of dNMPs adsorption and desorption events, on the overall translocation process and on the accuracy of the various calculated averaged quantities such as the PDFs of the time-of-flight of dNMPs over certain channel length. To further our understanding of the effect of the limited MD simulation time on the predicted PDFs of the time-of-flight we extended the  $E = 0.1$  V/nm smooth wall systems from 350 ns per mononucleotide to 700 ns per mononucleotide and calculated the corresponding PDFs of time-of-flight (see Figure 15b) and required distances to separate the time-of-flight distributions (see Table 1). As evident from Table 1 and Figure 15b by doubling the total MD simulation time the required distance to separate the dAMP from dGMP decreases from 105.2 to 78.9  $\mu\text{m}$ , and the corresponding PDFs for the times-of-flights undergo a shift toward smaller time-of-flight values. The ordering and the relative spacing between the four PDFs does not change much, and the corresponding minimum required analysis time per dNMP decreases just slightly from 8.8 to 7.8  $\mu\text{s}$ . This overall behavior indicates that 350 ns MD simulation time is long enough to at least capture the qualitative behavior of the flight time PDFs, and to obtain the required channel length and the minimum required analysis time with an uncertainty of less than 50%.

It is desirable to have all the time-of-flight distributions about the same distance from each other to keep the minimum analysis time per dNMP small. Figure 15b shows that this was the case for a smooth wall with  $E = 0.1$  V/nm, and the analysis time is about 8  $\mu\text{s}$ . For the rough walls with  $E = 0.1$  V/nm, the distributions for dAMP and dTMP were not close to those for dGMP and dCMP, and the analysis time was longer (about 46  $\mu\text{s}$ ). For a smooth wall with  $E = 0.0144$  V/nm, the distribution for dGMP was very far from the other three, and the analysis time was about 582  $\mu\text{s}$ . As with the channel length, the minimum analysis time per dNMP was also sensitive to the difference in the estimated mean velocities for the pair of dNMPs that were hardest to separate. Using the analysis mentioned previously in the context of channel length for the rough wall case gave a minimum value of about 15  $\mu\text{s}$ , a maximum value of about 341  $\mu\text{s}$ , and a median value of about 45  $\mu\text{s}$ . There may be a significant difference between the  $E = 0.0144$  V/nm case and the cases with  $E = 0.1$  V/nm.

## SUMMARY AND CONCLUSIONS

The electrophoretic transport of dNMPs in 3 nm wide slits composed of Lennard-Jones carbon atoms was studied using molecular dynamics simulations. The electric field strength ( $E$ ) was varied,  $E = 0.0, 0.0144, 0.1, 0.3$ , or  $0.6$  V/nm, with atomically smooth, but disordered slit walls. In one case with  $E = 0.1$  V/nm, slit walls with an RMS roughness on the order of the size of the dNMPs were also used. The effects of interactions of the dNMPs with the slit walls and the sodium ions in solution on the transport of the dNMPs were examined in detail. Minimum channel lengths and analysis times per dNMP required to separate time-of-flight distributions of the dNMPs were estimated from the molecular dynamics simulation results. These were put in the perspective of achieving successful discrimination between dNMPs for sequencing applications.

The dNMP trajectories consisted of multiple adsorptions and desorptions to and from the slit walls with the dNMPs tending

to adsorb with their nucleobase groups nearly flat on the surface. The orientations of the dNMP nucleobase groups relative to the wall surfaces as a function of distance from a slit wall during the adsorption and desorption processes were similar. The orientations were also similar as a function of  $E$  for  $E = 0.0, 0.0144$ , and  $0.1$  V/nm. This indicates that the mechanism of adsorption and desorption is not affected by the electric field if  $E$  is small enough.

Statistics related to adsorption and desorption were computed. Increased electric field strength with smooth walls decreased the fraction of the total time during which the dNMPs were adsorbed to the walls, decreased the mean time per adsorption event, increased the frequency of adsorption events, and increased the velocity of the dNMPs while adsorbed. Increased driving force made desorption more likely and sped up the sliding of the dNMPs on the slit walls. The mean distance traveled by the dNMPs in the direction of the driving force while adsorbed increased with increasing  $E$  up to  $E = 0.3$  V/nm, but it was about the same for  $E = 0.3$  and  $0.6$  V/nm due to the competing effects of increased velocity while adsorbed and decreased time per adsorption event with increased  $E$ . Using rough walls generally made desorption more likely (decreased mean times and distances per adsorption event) and slowed down the sliding of the dNMPs on the walls (decreased velocity while adsorbed). The fractions of the total time that the dNMPs were adsorbed decreased for all dNMPs, but not significantly for dTMP. This was due to the large increase in the frequency of adsorption events for dTMP; its high hydrophobicity made readsorption after desorption very fast. In general, the frequency of adsorption increased when using rough walls. The mean time per adsorption event for dTMP also decreased less than for the other dNMPs when comparing smooth and rough walls, again due to its high hydrophobicity. The velocity of the dNMPs in the direction of the driving force while desorbed was not a function of dNMP or wall roughness as expected. The mean time and distance per desorption event were not influenced by  $E$  or wall roughness, but decreased with increasing hydrophobicity of the nucleobase parts of the dNMPs due to faster readsorption for more hydrophobic dNMPs. The dNMP–wall interactions affected the frequency and duration of the dNMP adsorption and desorption periods as well as the dNMP velocities during those periods which helped to separate the dNMP time-of-flight distributions.

Transient ion association between the anionic phosphate group of the dNMPs and the sodium cations in solution was observed with the number of associated sodium ions varying from 0 to 3. The average number of associated sodium ions was around 1. Due to the transient nature of the association, the force on the dNMP–sodium complex due to the electric field also varied leading to changes in the dNMP velocity ranging from very fast with an association number of 0, to approximately zero with an association number of 2, and to even having the opposite sign with an association number of 3 (rare). The mean association numbers appeared to be a function of the electric field strength, but the differences were not significant considering the uncertainties. The dNMPs with purine nucleobases (dCMP and dTMP) had slightly fewer associated sodium ions on average compared to the dNMPs with pyrimidine nucleobases (dGMP and dTMP). Sodium association had a large effect on the instantaneous dNMP velocities, but little effect on the mean velocities and therefore helped little with separating their time-of-flight distributions.

The required channel lengths were on the order of 100  $\mu\text{m}$  for all of the cases studied in which all dNMPs were simulated. For  $E = 0.1 \text{ V/nm}$ , the minimum analysis time per dNMP was 8  $\mu\text{s}$  for the smooth wall case and 45  $\mu\text{s}$  for the rough wall case. Both the required channel lengths and analysis times per dNMP would of course be larger for realistic field strengths due to diffusional broadening of the flight time distributions, but it appears that smoother walls may be superior in that they might lead to faster analysis times.

The order of the mean velocities or times-of-flight was affected by the rough walls compared to the smooth walls. For smooth walls, the order of the times-of-flight was dCMP < dTMP < dAMP < dGMP; the larger dAMP and dGMP were slowed down more when adsorbed. For rough walls, the order of the times-of-flight was dAMP < dGMP < dCMP < dTMP; the dAMP and dGMP did not stay adsorbed as much and therefore moved faster overall since there were fewer favorable adsorption sites for them on rough walls. Walls with roughness having specific characteristics, or physically or chemically structured walls, might be useful for improving the separation of the dNMP time-of-flight distributions.

## ASSOCIATED CONTENT

### Supporting Information

The Supporting Information is available free of charge on the ACS Publications website at DOI: [10.1021/acs.jpcb.5b02798](https://doi.org/10.1021/acs.jpcb.5b02798).

Description of the construction of the rough slit walls, the definition of adsorption and desorption for rough walls, a description of the calculation of the aggregate existence autocorrelation functions and relaxation times, a description of the calculation of the required channel length and analysis time per dNMP, and a description of the calculation of uncertainties; additional plots of the nucleobase–wall surface angles, nucleobase–electric field angles, and  $\text{Na}^+–\text{P}$  radial distribution functions (PDF)

## AUTHOR INFORMATION

### Corresponding Author

\*Phone: 225-578-6488. Fax: 225-578-5924. E-mail: [dmoldo1@lsu.edu](mailto:dmoldo1@lsu.edu).

### Notes

The authors declare no competing financial interest.

## ACKNOWLEDGMENTS

This study is based upon work supported by National Science Foundation (Grants EPSCoR LA-SiGMA EPS-1003897 and CBET-1067583). Computer Resources were provided by LONI and HPC at LSU.

## REFERENCES

- (1) Luan, B. Q.; Peng, H. B.; Polonsky, S.; Rossnagel, S.; Stolovitzky, G.; Martyna, G. Base-by-Base Ratcheting of Single Stranded DNA through a Solid-State Nanopore. *Phys. Rev. Lett.* **2010**, *104*, 238103.
- (2) Astier, Y.; Braha, O.; Bayley, H. Toward Single Molecule DNA Sequencing: Direct Identification of Ribonucleoside and Deoxyribonucleoside 5'-Monophosphates by Using an Engineered Protein Nanopore Equipped with a Molecular Adapter. *J. Am. Chem. Soc.* **2006**, *128*, 1705–1710.
- (3) Clarke, J.; Wu, H. C.; Jayasinghe, L.; Patel, A.; Reid, S.; Bayley, H. Continuous Base Identification for Single-Molecule Nanopore DNA Sequencing. *Nat. Nanotechnol.* **2009**, *4*, 265–270.
- (4) Miles, B. N.; Ivanov, A. P.; Wilson, K. A.; Dogan, F.; Japrung, D.; Edel, J. B. Single Molecule Sensing with Solid-State Nanopores: Novel Materials, Methods, and Applications. *Chem. Soc. Rev.* **2013**, *42*, 15–28.
- (5) Haque, F.; Li, J.; Wu, H.-C.; Liang, X.-J.; Guo, P. Solid-State and Biological Nanopore for Real-Time Sensing of Single Chemical and Sequencing of DNA. *Nano Today* **2013**, *8*, 56–74.
- (6) Yang, Y.; Liu, R.; Xie, H.; Hui, Y.; Jiao, R.; Gong, Y.; Zhang, Y. Advances in Nanopore Sequencing Technology. *J. Nanosci. Nanotechnol.* **2013**, *13*, 4521–4538.
- (7) Nosik, V. L.; Rudakova, E. B. Prospects of Biomolecule Sequencing with the Techniques of Translocation through Nanopores: A Review. *Crystallogr. Rep.* **2013**, *58*, 805–821.
- (8) Ying, Y.-L.; Zhang, J.; Gao, R.; Long, Y.-T. Nanopore-Based Sequencing and Detection of Nucleic Acids. *Angew. Chem., Int. Ed.* **2013**, *52*, 13154–13161.
- (9) Novak, B. R.; Moldovan, D.; Nikitopoulos, D. E.; Soper, S. A. Distinguishing Single DNA Nucleotides Based on Their Times of Flight through Nanoslits: A Molecular Dynamics Simulation Study. *J. Phys. Chem. B* **2013**, *117*, 3271–3279.
- (10) Lee, J. W.; Meller, A. Rapid DNA Sequencing by Direct Nanoscale Reading of Nucleotide Bases on Individual DNA Chains. In *Perspectives in Bioanalysis*; Mitchelson, K. R., Ed.; Elsevier: Amsterdam, 2007; Vol. 2.
- (11) Deamer, D. W.; Branton, D. Characterization of Nucleic Acids by Nanopore Analysis. *Acc. Chem. Res.* **2002**, *35*, 817–825.
- (12) Kasianowicz, J. J.; Brandin, E.; Branton, D.; Deamer, D. W. Characterization of Individual Polynucleotide Molecules Using a Membrane Channel. *Proc. Natl. Acad. Sci. U. S. A.* **1996**, *93*, 13770–13773.
- (13) Tsutsui, M.; Taniguchi, M.; Yokota, K.; Kawai, T. Identifying Single Nucleotides by Tunnelling Current. *Nat. Nanotechnol.* **2010**, *5*, 286–290.
- (14) Fischbein, M. D.; Drndic, M. Sub-10 Nm Device Fabrication in a Transmission Electron Microscope. *Nano Lett.* **2007**, *7*, 1329–1337.
- (15) Zwolak, M.; Di Ventra, M. Electronic Signature of DNA Nucleotides Via Transverse Transport. *Nano Lett.* **2005**, *5*, 421–424.
- (16) Lagerqvist, J.; Zwolak, M.; Di Ventra, M. Fast DNA Sequencing Via Transverse Electronic Transport. *Nano Lett.* **2006**, *6*, 779–782.
- (17) Yokota, K.; Tsutsui, M.; Taniguchi, M. Electrode-Embedded Nanopores for Label-Free Single-Molecule Sequencing by Electric Currents. *RSC Adv.* **2014**, *4*, 15886–15899.
- (18) Healy, K.; Ray, V.; Willis, L. J.; Peterman, N.; Bartel, J.; Drndić, M. Fabrication and Characterization of Nanopores with Insulated Transverse Nanoelectrodes for DNA Sensing in Salt Solution. *Electrophoresis* **2012**, *33*, 3488–3496.
- (19) Fanget, A.; Traversi, F.; Khlybov, S.; Granjon, P.; Magrez, A.; Forró, L.; Radenovic, A. Nanopore Integrated Nanogaps for DNA Detection. *Nano Lett.* **2014**, *14*, 244–249.
- (20) He, Y. H.; Shao, L. B.; Scheicher, R. H.; Grigoriev, A.; Ahuja, R.; Long, S. B.; Ji, Z. Y.; Yu, Z. A.; Liu, M. Differential Conductance as a Promising Approach for Rapid DNA Sequencing with Nanopore-Embedded Electrodes. *Appl. Phys. Lett.* **2010**, *97*, 043701.
- (21) Sigalov, G.; Comer, J.; Timp, G.; Aksimentiev, A. Detection of DNA Sequences Using an Alternating Electric Field in a Nanopore Capacitor. *Nano Lett.* **2008**, *8*, S6–63.
- (22) Bobadilla, A. D.; Seminario, J. M. Assembly of a Noncovalent DNA Junction on Graphene Sheets and Electron Transport Characteristics. *J. Phys. Chem. C* **2013**, *117*, 26441–26453.
- (23) Puster, M.; Rodríguez-Manzo, J. A.; Balan, A.; Drndić, M. Toward Sensitive Graphene Nanoribbon–Nanopore Devices by Preventing Electron Beam-Induced Damage. *ACS Nano* **2013**, *7*, 11283–11289.
- (24) Traversi, F.; Raillon, C.; Benameur, S. M.; Liu, K.; Khlybov, S.; Tosun, M.; Krasnozhon, D.; Kis, A.; Radenovic, A. Detecting the Translocation of DNA through a Nanopore Using Graphene Nanoribbons. *Nat. Nanotechnol.* **2013**, *8*, 939–945.
- (25) Rezapour, M. R.; Rajan, A. C.; Kim, K. S. Molecular Sensing Using Armchair Graphene Nanoribbon. *J. Comput. Chem.* **2014**, *35*, 1916–1920.

- (26) Langecker, M.; Pedone, D.; Simmel, F. C.; Rant, U. Electrophoretic Time-of-Flight Measurements of Single DNA Molecules with Two Stacked Nanopores. *Nano Lett.* **2011**, *11*, 5002–5007.
- (27) Harms, Z. D.; Haywood, D. G.; Kneller, A. R.; Selzer, L.; Zlotnick, A.; Jacobson, S. C. Single-Particle Electrophoresis in Nanochannels. *Anal. Chem.* **2015**, *87*, 699–705.
- (28) Harms, Z. D.; Mogensen, K. B.; Nunes, P. S.; Zhou, K. M.; Hildenbrand, B. W.; Mitra, I.; Tan, Z. N.; Zlotnick, A.; Kutter, J. P.; Jacobson, S. C. Nanofluidic Devices with Two Pores in Series for Resistive-Pulse Sensing of Single Virus Capsids. *Anal. Chem.* **2011**, *83*, 9573–9578.
- (29) Davis, L. M.; Fairfield, F. R.; Harger, C. A.; Jett, J. H.; Keller, R. A.; Hahn, J. H.; Krakowski, L. A.; Marrone, B. L.; Martin, J. C.; Nutter, H. L.; et al. Rapid DNA Sequencing Based Upon Single Molecule Detection. *Genet. Anal.: Tech. Appl.* **1991**, *8*, 1–7.
- (30) Goodwin, P. M.; Cai, H.; Jett, J. H.; IshaugRiley, S. L.; Machara, N. P.; Semin, D. J.; Van Orden, A.; Keller, R. A. Application of Single Molecule Detection to DNA Sequencing. *Nucleosides Nucleotides* **1997**, *16*, 543–550.
- (31) Zhu, L.; Stryjewski, W. J.; Soper, S. A. Multiplexed Fluorescence Detection in Microfabricated Devices with Both Time-Resolved and Spectral-Discrimination Capabilities Using near-Infrared Fluorescence. *Anal. Biochem.* **2004**, *330*, 206–218.
- (32) McNally, B.; Singer, A.; Yu, Z.; Sun, Y.; Weng, Z.; Meller, A. Optical Recognition of Converted DNA Nucleotides for Single-Molecule DNA Sequencing Using Nanopore Arrays. *Nano Lett.* **2010**, *10*, 2237–2244.
- (33) Eid, J.; Fehr, A.; Gray, J.; Luong, K.; Lyle, J.; Otto, G.; Peluso, P.; Rank, D.; Baybayan, P.; Bettman, B.; et al. Real-Time DNA Sequencing from Single Polymerase Molecules. *Science* **2009**, *323*, 133–138.
- (34) Guy, A. T.; Piggot, T. J.; Khalid, S. Single-Stranded DNA within Nanopores: Conformational Dynamics and Implications for Sequencing; a Molecular Dynamics Simulation Study. *Biophys. J.* **2012**, *103*, 1028–1036.
- (35) Maglia, G.; Restrepo, M. R.; Mikhailova, E.; Bayley, H. Enhanced Translocation of Single DNA Molecules through Alpha-Hemolysin Nanopores by Manipulation of Internal Charge. *Proc. Natl. Acad. Sci. U. S. A.* **2008**, *105*, 19720–19725.
- (36) Rincon-Restrepo, M.; Milthallova, E.; Bayley, H.; Maglia, G. Controlled Translocation of Individual DNA Molecules through Protein Nanopores with Engineered Molecular Brakes. *Nano Lett.* **2011**, *11*, 746–750.
- (37) Wu, H. C.; Astier, Y.; Maglia, G.; Mikhailova, E.; Bayley, H. Protein Nanopores with Covalently Attached Molecular Adapters. *J. Am. Chem. Soc.* **2007**, *129*, 16142–16148.
- (38) Bhattacharya, S.; Derrington, I. M.; Pavlenok, M.; Niederweis, M.; Gundlach, J. H.; Aksimentiev, A. Molecular Dynamics Study of Mspa Arginine Mutants Predicts Slow DNA Translocations and Ion Current Blockades Indicative of DNA Sequence. *ACS Nano* **2012**, *6*, 6960–6968.
- (39) Langecker, M.; Arnaut, V.; Martin, T. G.; List, J.; Renner, S.; Mayer, M.; Dietz, H.; Simmel, F. C. Synthetic Lipid Membrane Channels Formed by Designed DNA Nanostructures. *Science* **2012**, *338*, 932–936.
- (40) Bell, N. A. W.; Keyser, U. F. Nanopores Formed by DNA Origami: A Review. *FEBS Lett.* **2014**, *588*, 3564–3570.
- (41) Liu, L.; Yang, C.; Zhao, K.; Li, J.; Wu, H.-C. Ultrashort Single-Walled Carbon Nanotubes in a Lipid Bilayer as a New Nanopore Sensor. *Nat. Commun.* **2013**, *4*, 2989.
- (42) Rhee, M.; Burns, M. A. Nanopore Sequencing Technology: Research Trends and Applications. *Trends Biotechnol.* **2006**, *24*, 580–586.
- (43) Storm, A. J.; Chen, J. H.; Ling, X. S.; Zandbergen, H. W.; Dekker, C. Fabrication of Solid-State Nanopores with Single-Nanometre Precision. *Nat. Mater.* **2003**, *2*, 537–540.
- (44) Larkin, J.; Henley, R.; Bell, D. C.; Cohen-Karni, T.; Rosenstein, J. K.; Wanunu, M. Slow DNA Transport through Nanopores in Hafnium Oxide Membranes. *ACS Nano* **2013**, *7*, 10121–10128.
- (45) Zhou, Z.; Hu, Y.; Wang, H.; Xu, Z.; Wang, W.; Bai, X.; Shan, X.; Lu, X. DNA Translocation through Hydrophilic Nanopore in Hexagonal Boron Nitride. *Sci. Rep.* **2013**, *3*, 3287.
- (46) Liu, S.; Lu, B.; Zhao, Q.; Li, J.; Gao, T.; Chen, Y.; Zhang, Y.; Liu, Z.; Fan, Z.; Yang, F.; et al. Boron Nitride Nanopores: Highly Sensitive DNA Single-Molecule Detectors. *Adv. Mater.* **2013**, *25*, 4549–4554.
- (47) Wells, D. B.; Belkin, M.; Comer, J.; Aksimentiev, A. Assessing Graphene Nanopores for Sequencing DNA. *Nano Lett.* **2012**, *12*, 4117–4123.
- (48) Wang, Y.; Yu, X. F.; Liu, Y. Y.; Xie, X.; Cheng, X. L.; Huang, S. M.; Wang, Z. M. Fabrication of Graphene Nanopores and a Preliminary Study on Lambda-DNA Translocation. *Huaxue Xuebao* **2014**, *72*, 378–381.
- (49) Schneider, G. F.; Kowalczyk, S. W.; Calado, V. E.; Pandraud, G.; Zandbergen, H. W.; Vandersypen, L. M. K.; Dekker, C. DNA Translocation through Graphene Nanopores. *Nano Lett.* **2010**, *10*, 3163–3167.
- (50) Garaj, S.; Hubbard, W.; Reina, A.; Kong, J.; Branton, D.; Golovchenko, J. A. Graphene as a Subnanometre Trans-Electrode Membrane. *Nature* **2010**, *467*, 190–U173.
- (51) Merchant, C. A.; Drndić, M. Graphene Nanopore Devices for DNA Sensing. In *Nanopore-Based Technology*; Springer: New York, 2012; Vol. 870, pp 211–226. DOI: 10.1007/978-1-61779-773-6\_12.
- (52) Sadeghi, H.; Algaragholy, L.; Pope, T.; Bailey, S.; Visontai, D.; Manrique, D.; Ferrer, J.; Garcia-Suarez, V.; Sangtarash, S.; Lambert, C. J. Graphene Sculpture Nanopores for DNA Nucleobase Sensing. *J. Phys. Chem. B* **2014**, *118*, 6908–6914.
- (53) Liang, L.; Zhang, Z.; Shen, J.; Zhe, K.; Wang, Q.; Wu, T.; Agren, H.; Tu, Y. Theoretical Studies on the Dynamics of DNA Fragment Translocation through Multilayer Graphene Nanopores. *RSC Adv.* **2014**, *4*, 50494–50502.
- (54) Farimani, A. B.; Min, K.; Aluru, N. R. DNA Base Detection Using a Single-Layer MoS<sub>2</sub>. *ACS Nano* **2014**, *8*, 7914–7922.
- (55) Oliver-Calixte, N. J.; Uba, F. I.; Battle, K. N.; Weerakoon-Ratnayake, K. M.; Soper, S. A. Immobilization of Lambda Exonuclease onto Polymer Micropillar Arrays for the Solid-Phase Digestion of DsDNAs. *Anal. Chem.* **2014**, *86*, 4447–4454.
- (56) Menard, L. D.; Ramsey, J. M. Fabrication of Sub-5 nm Nanochannels in Insulating Substrates Using Focused Ion Beam Milling. *Nano Lett.* **2011**, *11*, 512–517.
- (57) Humphrey, W.; Dalke, A.; Schulten, K. Vmd: Visual Molecular Dynamics. *J. Mol. Graphics* **1996**, *14*, 33–38.
- (58) Foloppe, N.; MacKerell, A. D. All-Atom Empirical Force Field for Nucleic Acids: I. Parameter Optimization Based on Small Molecule and Condensed Phase Macromolecular Target Data. *J. Comput. Chem.* **2000**, *21*, 86–104.
- (59) *Nucleic Acids in Chemistry and Biology*; Blackburn, G. M., Gait, M. J., Eds.; IRL Press: Oxford, 1990.
- (60) Yeh, I. C.; Berkowitz, M. L. Ewald Summation for Systems with Slab Geometry. *J. Chem. Phys.* **1999**, *111*, 3155–3162.
- (61) Czarnecka, J.; Cieslak, M.; Michal, K. Application of Solid Phase Extraction and High-Performance Liquid Chromatography to Qualitative and Quantitative Analysis of Nucleotides and Nucleosides in Human Cerebrospinal Fluid. *J. Chromatogr. B: Anal. Technol. Biomed. Life Sci.* **2005**, *822*, 85–90.
- (62) Perrett, D.; Bhusate, L.; Patel, J.; Herbert, K. Comparative Performance of Ion-Exchange and Ion-Paired Reversed Phase High-Performance Liquid-Chromatography for the Determination of Nucleotides in Biological Samples. *Biomed. Chromatogr.* **1991**, *5*, 207–211.
- (63) Castillo-Fernandez, O.; Salieb-Beugelaar, G. B.; van Nieuwkastele, J. W.; Bomer, J. G.; Arundell, M.; Samitier, J.; van den Berg, A.; Eijkel, J. C. T. Electrokinetic DNA Transport in 20 nm-High Nanoslits: Evidence for Movement through a Wall-Adsorbed Polymer Nanogel. *Electrophoresis* **2011**, *32*, 2402–2409.

- (64) Mumper, R. J.; Wang, J. J.; Klakamp, S. L.; Nitta, H.; Anwer, K.; Tagliaferri, F.; Rolland, A. P. Protective Interactive Noncondensing (Pinc) Polymers for Enhanced Plasmid Distribution and Expression in Rat Skeletal Muscle. *J. Controlled Release* **1998**, *52*, 191–203.
- (65) Kang, S. H.; Shortreed, M. R.; Yeung, E. S. Real-Time Dynamics of Single-DNA Molecules Undergoing Adsorption and Desorption at Liquid–Solid Interfaces. *Anal. Chem.* **2001**, *73*, 1091–1099.
- (66) Wu, L. Z.; Liu, H.; Zhao, W. Y.; Wang, L.; Hou, C. R.; Liu, Q. J.; Lu, Z. H. Electrically Facilitated Translocation of Protein through Solid Nanopore. *Nanoscale Res. Lett.* **2014**, *9*, 140.
- (67) Shih, P.; Pedersen, L. G.; Gibbs, P. R.; Wolfenden, R. Hydrophobicities of the Nucleic Acid Bases: Distribution Coefficients from Water to Cyclohexane. *J. Mol. Biol.* **1998**, *280*, 421–430.
- (68) Munoz-Muriedas, J.; Barril, X.; Lopez, J. M.; Orozco, M.; Luque, F. J. A Hydrophobic Similarity Analysis of Solvation Effects on Nucleic Acid Bases. *J. Mol. Model.* **2007**, *13*, 357–365.
- (69) MacKerell, A. D. Influence of Magnesium Ions on Duplex DNA Structural, Dynamic, and Solvation Properties. *J. Phys. Chem. B* **1997**, *101*, 646–650.
- (70) Mocci, F.; Laaksonen, A. Insight into Nucleic Acid Counterion Interactions from inside Molecular Dynamics Simulations Is "Worth Its Salt". *Soft Matter* **2012**, *8*, 9268–9284.
- (71) Shen, X.; Gu, B.; Che, S. A.; Zhang, F. S. Solvent Effects on the Conformation of DNA Dodecamer Segment: A Simulation Study. *J. Chem. Phys.* **2011**, *135*, 034509.
- (72) Musheev, M. U.; Kanoatov, M.; Krylov, S. N. Non-Uniform Velocity of Homogeneous DNA in a Uniform Electric Field: Consequence of Electric-Field-Induced Slow Dissociation of Highly Stable DNA-Counterion Complexes. *J. Am. Chem. Soc.* **2013**, *135*, 8041–8046.
- (73) Kowalczyk, S. W.; Wells, D. B.; Aksimentiev, A.; Dekker, C. Slowing Down DNA Translocation through a Nanopore in Lithium Chloride. *Nano Lett.* **2012**, *12*, 1038–1044.
- (74) Brehm, M.; Kirchner, B. Travis - a Free Analyzer and Visualizer for Monte Carlo and Molecular Dynamics Trajectories. *J. Chem. Inf. Model.* **2011**, *51*, 2007–2023.
- (75) Kunsch, H. R. The Jackknife and the Bootstrap for General Stationary Observations. *Annals of Statistics* **1989**, *17*, 1217–1241.